TITLE: Biophysically relevant network model of the piriform cortex predicts odor frequency encoding using network mechanisms

Abbreviated Title: Piriform cortex encodes odor frequency

Authors: Ankit Kumar[1], Om Chaudhari[2], Manan Jindal[3], Ashutosh Modi[2], Debanjan Dasgupta[1*]

Affiliations: [1]Department of Biological Sciences and Bioengineering, Indian Institute of Technology, Kanpur, 208016, India; [2]Department of Computer Science and Engineering, Indian Institute of Technology, Kanpur, 208016, India; and [3]Department of Electrical Engineering, Indian Institute of Technology, Kanpur, 208016, India

***To whom correspondence should be addressed:** Debanjan Dasgupta at debanjand@iitk.ac.in

Number of text pages: 36

Number of figures: 9

Number of tables: 4

Number of words for abstract: 248

Number of words for introduction: 601

Number of words for discussion: 1364

Conflict of interest: The authors declare no competing financial interests.

Acknowledgements: The work was supported by a Ramalingaswami fellowship from the Department of Biotechnology, India (BT/RLF/Re-entry/14/2022) and a startup grant from the Indian Institute of Technology (IIT) Kanpur awarded to Debanjan Dasgupta. This research utilized the High-Performance Cluster (Param Sanganak) facilities at the Computer Centre, IIT Kanpur.

Abstract

Olfactory-guided animals utilize fast concentration fluctuations in turbulent odor plumes to perceive olfactory landscapes. Recent studies demonstrate that the olfactory bulb (OB) encodes such temporal features present in natural odor stimuli. However, whether this temporal information is encoded in the piriform cortex (PCx), the primary cortical target of OB projections, remains unknown. Here, we developed a biophysically relevant PCx network model and simulated it using previously recorded *in vivo* activities of mitral and tufted cells from OB in response to 2Hz and 20Hz odor frequencies for three odor mixtures. Analysis of the pyramidal cells' (PYRs) activity during the initial 500ms of odor stimulation revealed that 4.4-11.8% of cells exhibited significantly different average firing rates for the two different frequencies. Furthermore, 1D convolutional neural network (CNN) models trained and tested on PYRs' activities achieved discrimination accuracies of 73-95%. However, cells showing significant frequency discrimination contributed similarly to CNN performance as the non-discriminating cells. Using virtual synaptic knockout models, we found that eliminating either feedback or feedforward inhibition onto PYRs improved CNN decoding accuracy across all odor conditions. Conversely, eliminating recurrent excitation among pyramidal neurons or eliminating recurrent inhibition among both interneuron types simultaneously degraded CNN accuracy. Removing recurrent connections within individual interneuron populations had minimal effects on the performance. Our PCx model demonstrates that it can discriminate between 2Hz and 20Hz odor stimuli, with a bidirectional capability of performance modulation by specific circuit motifs. These findings predict that the piriform cortex encodes and processes temporal features of odor stimuli.

Significance Statement

Temporal dynamics of odor concentration in odor plumes carry crucial spatial information for olfactory-guided animals. Here, we simulated a biophysically relevant network model of the piriform cortex to show that the network differentially encodes odor frequencies at 2Hz and 20Hz. Using 1D convolutional neural networks, we demonstrate that the odor frequency response decoding was well

above chance level and broadly distributed among piriform cortex output neurons. Furthermore, we show that various circuit motifs within the network impact its frequency encoding capacity, an effect that could not be replicated by merely altering the baseline activity of pyramidal cells. Overall, our results predict that the piriform cortex network can discriminate odor frequencies, which can be modulated bidirectionally by specific network attributes.

Introduction

In natural olfactory environment, odorant molecules travel as odor plumes due to the turbulence of natural airflow (Murlis et al., 2003; Koehl, 2006; Celani et al., 2014; Ackels et al., 2021). These odor plumes are characterized by rapid fluctuations in the concentration of odorant molecules over space and time (Mylne and Mason, 1991; Shralman and Siggia, 2000; Celani et al., 2014; Marin et al., 2021a; Crimaldi et al., 2022). These odor plumes carry crucial spatial information about odor source location, embedded in their temporal structure (Murlis et al., 2003; Ackels et al., 2021; Marin et al., 2021b). Olfactory-guided animals can perceive the temporal structure of odors (Murlis et al., 2003; Szyszka, 2005; Ackels et al., 2021; Marin et al., 2021b; Gumaste et al., 2024), and recent reports indicate that humans can perceive such stimuli as well (Caprio and Derby, 2008; Wu et al., 2024). Early olfactory regions, like the antennal lobe in insects (Vickers and Baker, 1994; Laurent et al., 1996; Vickers, 2000; Vickers et al., 2001; Huston et al., 2015; Lucas et al., 2019) and the olfactory bulb (OB) in mammals, encode these temporal features (Dasgupta et al., 2022; Lewis et al., 2024).

Owing to the slow signal transduction through GPCR-based odorant receptors, olfaction has largely been thought to be devoid of high-frequency temporal features of odor stimuli (Duchamp-Viret et al., 1999). However, studies in invertebrates (Vickers et al., 2001; Huston et al., 2015) and more recently in mice (Ackels et al., 2021; Crimaldi et al., 2022; Dasgupta et al., 2022; Gumaste et al., 2024; Lewis et al., 2024) and humans (Stern et al., 2018a) have shown that different temporal features of odor stimuli can be perceived and encoded at least in the early olfactory system. Nevertheless, it is unknown how the temporal frequency of fluctuating odor stimuli is encoded in cortical areas of the olfactory pathway, particularly the piriform cortex (PCx). The PCx has largely been associated with

encoding of odor identity (Bolding et al., 2020) and intensity (Bolding and Franks, 2017). The recurrent connectivity in the PCx together with the different inhibitory connections has been associated with olfactory sensory processing (Franks et al., 2011a) as well as odor-associated memory formation (Nagappan and Franks, 2021). Moreover, PCx, through its cortical feedback axons, provides the OB with efficiently formatted and decorrelated information about diverse odorant Mixtures and concentrations (Zak et al., 2024). However, we completely lack an understanding of whether PCx's recurrent circuitry is capable of discriminating odor frequency. Hence, given the importance of odor temporal information in various ethological behaviors and the known involvement of the olfactory cortex (Fischler-Ruiz et al., 2021; Mori and Sakano, 2021), we investigated whether the PCx encodes different temporal features present in naturalistic odor stimuli.

To investigate this, we developed a biophysically constrained network model of the PCx. We analyzed pyramidal cells' activity in response to three odorant mixtures presented at frequencies of 2Hz and 20Hz. Additionally, we simulated various PCx synaptic knockout models to determine the extent to which each circuit motif influences the network's frequency encoding capacity. Our findings demonstrate that the PCx network can effectively discriminate between 2Hz and 20Hz odor frequencies. Eliminating direct feedforward or feedback inhibition onto pyramidal cells enhanced the frequency decoding capacity of the PCx network model, whereas removing recurrent excitation onto pyramidal cells or disinhibition among both feedforward and feedback interneurons impaired this capacity. In contrast, the odor frequency decoding accuracy was robust to synaptic disconnections of the intra-feedforward or intra-feedback interneurons. Our predictions indicate that odor frequency discrimination in the PCx is largely a network property that can be modulated bidirectionally by its synaptic connections.

Materials and Methods

Model

The code was written in Python using the NEURON 8.0.2 simulation environment (Carnevale and

Hines, 2005) and executed using Conda/Virtual Environments. The integration time step for the simulations was 0.025ms.

Model Architecture

The piriform cortex model consisted of three types of cells: 500 excitatory pyramidal cells (PYRs), 50 feedforward inhibitory neurons (FFINs), and 50 feedback inhibitory neurons (FBINs). All synaptic connections within the network were randomly assigned, regardless of cell location. Previously recorded *in vivo* activity from 20-50 unique mitral/tufted cells (M/Ts) from the olfactory bulb in response to different stimulus conditions was used as input to simulate the PCx network model. These spiking activities were replicated as needed to generate an M/T cell population comprising ~22.5% of PYRs. Each pyramidal cell received input from 20% of mitral cells, as previously determined (Linster et al., 2009). Each pyramidal cell was connected to 20% of the total pyramidal cell population (Linster et al., 2009) through proximal apical dendrites (Franks et al., 2011b). The FFINs projected to the distal apical dendrites of pyramidal neurons (Poo and Isaacson, 2009; Isaacson, 2010; Stokes and Isaacson, 2010a). Each PYR was inhibited by 30% of the FFINs (Stokes and Isaacson, 2010b). Each FFIN received inputs from 40% of M/T cells (Poo and Isaacson, 2009; Stokes and Isaacson, 2010a). Each FBIN was excited by 18% of the PYRs and each PYR was inhibited by 35% of the FBIN network through somatic inhibition (Stokes and Isaacson, 2010a). Each FBIN received inhibitory inputs from 10% of FBINs, while each FFIN received inhibitory inputs from 40% of FFINs.

Neuron and Electrophysiological parameters

Pyramidal (PYR) neuron model:

Each PYR was composed of a soma and five dendritic sections. The length and diameter of the somatic section were both 29 µm. The length of all dendritic sections was 100µm. The diameters of all dendritic sections 1 to 5 were 2.57, 1.77, 1.2, 0.8, and 0.5 µm, respectively (Fig. S1A). Here, dendritic section 5 was considered the distal apical dendrite. The charge balance equation for each neuronal compartment is described by:

$$C_M \frac{dV}{dt} + I_K = I_A \qquad (1)$$

Where:

C_M is 1 μF/cm^2

V is membrane voltage

I_K is the sum of ionic currents that pass through the membrane and

I_A is the current entering from adjacent regions.

Equations governing I_K are defined explicitly in the mod file of each ion channel mechanism. Ion channel mechanisms (*.mod files) can be compiled using NRNIVMODL of NEURON. The value of axial resistance (R_a) for each section of all neuronal types was 173 Ωcm. Each PYR section had sodium and delayed rectifier potassium channel mechanisms adopted from Migliore et al. (1999). Leak channels in PYRs were implemented using NEURON's built-in "leak" distributed mechanism. The maximum conductance of sodium, potassium, and leak ion channels was 0.5, 0.06, and 0.003 S/cm^2, respectively. The reversal potential of sodium, potassium, and leak ion channels was 50 mV, -85 mV, and -75 mV, respectively. The resting membrane potential (RMP) of PYRs was -74.1 ± 8.6 mV (mean ± SD) (Bathellier et al., 2009). The input resistance of PYR soma and its dendritic sections 1 to 5 were 79.84, 80.28, 84.94, 99.36, 137.58, and 246.18 MΩ, respectively (Fig. S2B) based on experimental data (Bathellier et al., 2009). The baseline spike rate of soma, dend1, dend2, dend3, dend4, and dend5 was 2.22±0.98, 2.21±1.27, 2.32±1.2, 2.19±1.16, 2.2±1.4, and 2.67±1.59 Hz (mean ± SD), respectively (Fig. S2D). The f-I curve (firing frequency vs. injected current) of PYRs (Fig. S2E) closely matched previous experimental results (Ikeda et al., 2018). PYR baseline noise was modeled using NEURON's "INGAUSS" mechanism with mean ± SD = 0 ± 0.092, which generates action potentials at a specified frequency. For a concise overview of these parameters refer to Table 1.

Feedforward (FF) and Feedback (FB) interneuron model:

FFINs and FBINs are represented as single somatic compartments. The length and diameter of FFINs were both 85 μm, while those of FBINs were 68 μm (Fig. S1B-C). The charge balance equation in the compartments of both neuronal types is described by the same Equation (1). FFINs

and FBINs have sodium, potassium, and leak channel mechanisms adapted from Wang and Buzsáki (1996). For FFINs, the maximum conductance of sodium, potassium, and leak channels was 0.05 S/cm^2, 0.015 S/cm^2, and 0.000048 S/cm^2, respectively. The reversal potentials for sodium, potassium, and leak channels were 55 mV, -90 mV, and -72 mV, respectively. For FBINs, the maximum conductance of sodium, potassium, and leak channels was 0.05, 0.01, and 0.00014 S/cm^2, respectively. The reversal potentials for sodium, potassium, and leak channels was 55 mV, -90 mV, and -78 mV, respectively. The resting membrane potential of FFINs and FBINs were -72 ± 5.9 mV and -77.8 ± 11.3 mV (mean ± SD), respectively (Suzuki and Bekkers, 2010). The estimated input resistance of FFINs and FBINs were 93.36 MΩ (Fig. S3B(III)) and 50.29 MΩ (Fig. S4B(III)) respectively (Suzuki and Bekkers, 2010). The current vs. firing frequency plots estimated from FFINs (Fig. S3D) and FBINs (Fig. S4D) corroborated previous experimental results (Suzuki and Bekkers, 2010). FFINs' and FBINs' baseline noise was also modeled using NEURON's "INGAUSS" function with 0 ± 2.3 and 0 ± 5 (mean ± SD), respectively. The baseline firing rates of FFINs and FBINs were 2 ± 1.14 Hz (Fig. S3F) and 6.55 ± 2.11 Hz (Fig. S4F), respectively. Simulations were conducted at a temperature of 33°C.

The somatic compartment of each cell type acts as an integration site for all inputs and generates spikes. This conceptual model of NEURON is based on the spike-triggered synaptic transmission in which a spike detected at the presynaptic terminal using a NetCon object causes conductance change at the postsynaptic terminal. A NetCon object connects a presynaptic variable, such as voltage, to a target synapse with a desired delay and weight (Carnevale and Hines, 2005). Every synapse was modeled using a two-state kinetic scheme described by rise time Tau1 and decay time constant Tau2 and a reversal potential, E_N. All synapses were modeled using the NEURON's in-built "Exp2Syn" function. Synaptic latencies across different connection types were consistent with findings from Suzuki and Bekkers (2011). The synaptic parameters (Tau1 and Tau2) were adjusted to provide the best fit for the target PSPs (Stern et al., 2018b). Please refer to Table 2 for the comprehensive list of parameters.

Odorant Stimulation

To stimulate the PCx network model, we used previously recorded *in vivo* spiking activity from individual mitral and tufted cells (M/Ts) as described in Dasgupta et al. (2022a). The OB activity corresponded to three different odor Mixtures (A: ethyl butyrate and 2-hexanone (1:1); B: isopentyl acetate and eucalyptol (1:1); and Mix: A and B (1:1)) presented at two different frequencies (2Hz and 20Hz). Each odorant condition was simulated for 6 seconds: 2 seconds baseline, 2 seconds odor stimulation, and 2 seconds post-stimulation. For each odorant condition, 336 trials were conducted, during which the synaptic connections within the PCx network model were kept constant. Synaptic inputs from M/Ts to PYRs and FFINs were randomized across trials to introduce trial-to-trial variability. Baseline spiking in every cell of the piriform cortex generated additional trial-to-trial variability and stochasticity in the model.

Statistical Analysis

Heat map of statistically significant cells

Statistics were computed in MATLAB. To analyze the model's response, spiking data from PYRs were collected for each odorant condition (odor A, B, and Mix at 2Hz and 20Hz) over 336 trials, since PYRs are the primary output neurons of the piriform cortex. For each trial of a given odorant condition, the activity of all PYRs was converted to firing frequencies using a bin size of 50ms. Mean firing frequency for each neuron was calculated across four post-stimulus time windows: 0.5s, 1s, 1.5s, and 2s. Average baseline firing was calculated during a 500-1500ms time window of the pre-stimulation period. For each neuron, baseline-corrected firing rates were statistically compared using two-tailed t-tests ($p < 0.05$). We performed two sets of comparisons: (1) odor identity (e.g., A vs. B, Mix vs. A, and Mix vs. B) and (2) odor frequency (2Hz vs. 20Hz) for each odor.

Analysis of spiking data

Input resistance was calculated from the slope of the steady-state voltage response vs. subthreshold current steps graph. Action potential threshold was defined as the membrane potential (V_m) at which dV_m/dt first exceeded 20 V/s. Baseline firing rate was calculated as mean ± SD of the number of action potentials generated spontaneously per second over a duration of 1.5s in 100 trials.

f-I plots were generated by quantifying the number of action potentials as a function of injected current steps over 1s for a specific cell type without noise being added. EPSP and IPSP for a specific synaptic connection were determined as the peak rise or decline in V_m from its resting membrane potential (RMP), respectively.

1D CNN

We employed 1D convolutional neural networks (CNNs) to perform binary classification of odor stimuli based on PYRs' spiking activity (Fig. 2A). For this, spike trains were binned into non-overlapping 20ms windows, producing binary activity vectors for each neuron based on whether a neuron spiked at least once within the specified time bin. Hence, the dimension of our dataset for any binary classification task would be 672*N*100 where 672 (2*336) is the number of trials, N is the size of the PYR population used for the particular classification, and 100 is the number of time bins (2000/20). Once the dataset is prepared, it is classified into training and testing, with 60% and 40% of the data, respectively. Input to our 1D CNN model was fed in the form of 100*N. In 1D CNN, convolution is applied in 1 dimension only, which in our case is time. The convolutional layer applied temporal filters (kernel size = 3) across the input to extract time-dependent features. Convolution is a linear operation that involves multiplying the inputs with a set of weights. In our case, inputs are multiplied with the two-dimensional array of weights, known as a filter, of dimension 3*N where 3 is the kernel size. This operation assigns a unique value to each pass, resulting in a feature map with a dimension of 100. Once computed, each value in the feature map is passed to the ReLU (Rectified Linear Unit) activation function. Rectified linear unit is a linear activation function that transforms negative input to zero and outputs the same input for positive input. Convolutional neural networks may likely overfit the training data, so, a regularization technique that sets the inputs to 0 for some fraction of neurons during the training phase is used to prevent the model from overfitting. Finally, the outputs from the 1D convolutional layer are flattened into a 1D vector using a flatten layer before the fully connected dense layers. These dense/fully connected layers, after application of the activation function (Softmax), map the results to the probability distribution of classes. Our 1D CNN consists of 2 convolution layers and 2 dense layers with a drop-out rate of 0.3 applied after each layer as shown

in Fig. 2A. The first convolutional layer consists of 128 filters with a kernel size of 3 along with the ReLU activation function. This layer takes the input sample in the form of 100*N and transforms the sample into 100*128. A dropout rate of 0.3 was applied after each layer to mitigate overfitting. It is then followed by another convolutional layer consisting of 128 filters with a kernel size of 3. The output from this layer is then flattened into a 1D vector. Finally, 2 dense layers were employed using the ReLU activation function followed by a final dense layer with the Softmax activation function for predicting the probability of the target stimulus. The model was trained using the Adam optimizer for weight optimization and categorical cross-entropy as the loss function. During training, the number of epochs and batch size were 75 and 32, respectively. To prevent overfitting and unnecessary training, early stopping was implemented based on validation loss, with a patience parameter of 5 epochs. We conducted a series of experiments to identify the parameters that optimized the CNN's classification performance.

Accuracy vs. Cell Number

To quantify how decoding performance scales with neuronal population size, 1D CNNs were trained and tested on PYR subsets ranging from 50 to 500 neurons, in 50-neuron increments. For statistical robustness, 144 independent trials were conducted per population size. In each iteration, neurons were randomly sampled from the entire PYR population of 500 neurons, and data (i.e., 2*336 trials) were randomly split into training (60%) and testing (40%) sets. To establish a baseline for chance-level performance, we trained the model on datasets where the stimulus labels were randomly shuffled. This disrupted any real relationship between spiking patterns and stimulus identity while preserving the overall distribution of spike data. Decoding accuracy on the test set was recorded for each trial under both actual and shuffled-label conditions. Finally, the results were averaged across trials to compute mean accuracy and standard deviation for each population size. This analysis identified the marginal benefit of including additional neurons and helped determine whether performance plateaued at larger population sizes.

Determining cell importance

The importance of individual neurons for binary classification was quantified using negative cross-entropy loss (log likelihood) of the CNN model. Log-likelihood measures how well our model's probability predictions align with the true class labels (1 or 0). Mathematically, it is calculated as the sum of log predicted probabilities of true class labels in the test set. Higher values of log-likelihood indicate better model performance, meaning stronger alignment between predictions and actual class labels. The odor frequency trials of PYRs were randomly divided into two sets: a training set (70%) and a test set (30%). The CNN models were trained and tested on the data corresponding to odor stimulation period (i.e., 2-4s) and then log-likelihood was calculated. Then we replaced a given neuron's stimulus response activity with its baseline/pre-stimulus activity in the test set and again calculated the log-likelihood. The impact of this perturbation was measured by the difference between log-likelihood of the model for intact and perturbed conditions (ΔLL). A substantial reduction indicated that the neuron was critical for decoding. We performed this analysis for all 500 PYRs one at a time. Neuron importance score was defined as the mean of ΔLL across all 300 iterations, with higher values indicating greater contribution to stimulus discrimination. Finally, neurons were ranked by their mean importance scores, revealing their relative importance to the model's performance. This procedure was performed separately for each experimental condition (A, B, and Mix). CNN architecture for this analysis was largely the same as outlined above except the number of epochs during training was 15 to avoid overfitting.

Accuracy using baseline firing data

To evaluate the model's behavior in the absence of stimulus, we trained and tested the model exclusively on baseline firing data (0–2s) of all 500 PYRs using the same CNN architecture and method outlined above. This experiment-tested whether the model learned any spurious patterns not directly related to the stimulus (Fig. S5). A total of 144 iterations were conducted, with each iteration involving a random 60%/40% train-test split.

PYRs population baseline firing rate

Spike data from all 500 pyramidal neurons were binned into 2000ms time windows and converted to firing rates (Hz) for all six odor conditions across 336 trials. Population baseline firing rates across all

network conditions were calculated by averaging the firing rate during the first time bin (0-2000ms, i.e., the baseline period) across all neurons, trials, and odor conditions. Data were analyzed using custom MATLAB functions, with mean ± standard deviation computed across all network conditions.

Code Accessibility

Source codes are available at https://github.com/ankitbishnoe29/Piriform-Cortex-network-Project.git

Results

To investigate how odor frequency is represented and transformed in the piriform cortex (PCx), we constructed a biophysically relevant network model comprising of 500 pyramidal neurons (PYRs), 50 feedforward interneurons (FFINs), and 50 feedback interneurons (FBINs). The model's architecture and connection probabilities were based on experimental data from rodents (Bekkers and Suzuki, 2013; de Almeida et al., 2013; Stern et al., 2018b). The network received olfactory bulb (OB) input using the spiking activity data that had been previously recorded from single mitral and tufted cells (M/Ts) *in vivo* as described in Dasgupta et al. (2022a). The OB activity was in response to three different odor Mixtures (A: ethyl butyrate and 2-hexanone (1:1); B: isopentyl acetate and eucalyptol (1:1); Mix: A and B (1:1)) presented at two frequencies (2Hz and 20Hz). The model was simulated using the NEURON environment for 6s (2s baseline followed by 2s of odor stimulation and 2s of post-stimulation).

Each PYR received excitatory inputs from a randomly chosen 20% of the M/Ts population and 20% of the remaining PYR population. These selections followed a uniform probability distribution. The FFINs received excitatory inputs from OB neurons and provided feedforward inhibition onto both PYRs and other FFINs. The FBINs received excitatory input from the PYRs and in turn provided feedback inhibition onto the PYRs and other FBINs. Parameter details are provided in the Materials and Methods section.

Each PYR was modeled to have a soma connected to an apical dendritic trunk made of five dendritic sections (Fig. S1A). The FFINs and FBINs were modeled to have just a single somatic compartment (Fig. S1B-C). The resting membrane potentials of PYRs, FFINs, and FBINs were -74.1

± 8.6 mV, -72 ± 5.9 mV, and -77.8 ± 11.3 mV, respectively. This corroborated previous experimental findings (Bathellier et al., 2009; Suzuki and Bekkers, 2010). The PYRs, FFINs and FBINs (Fig. S2E; Fig S3D; Fig S4D) showed similar action potential firing profiles compared to experimentally observed recordings (Suzuki and Bekkers, 2010; Ikeda et al., 2018). The estimated input resistance values measured from the soma and the dendrites of PYRs (79.84, 80.28, 84.94, 99.36, 137.58, and 246.18 MΩ from the soma and dend1 to dend5, respectively) (Fig. S2B) were consistent with experimental findings (Bathellier et al., 2009). The input resistance measured from the FFINs and the FBINs was 93.36 MΩ (Fig. S3B(III)) and 50.29 MΩ (Fig. S4B(III)), respectively (Suzuki and Bekkers, 2010).

Pyramidal neurons of the PCx can discriminate between 2Hz and 20Hz odor stimuli

We collected spike timings from PYRs across 336 trials for each odorant condition. These data were converted into average spiking frequencies for both the initial 500ms and the entire 2s odor stimulation period. We then subtracted the average baseline firing frequency from these values and compared them between pairs of different odor conditions to identify odor identity-discriminating cells and odor frequency-discriminating cells.

Based on the initial 500ms of the 2Hz odor stimulation period, 20, 31, and 36 out of 500 cells could statistically discriminate between Mix vs. A, A vs. B, and Mix vs. B, respectively ($p<0.05$, two-tailed t-test; Fig. 1C and H). For the 20Hz condition, 42, 96, and 37 out of 500 cells could statistically discriminate between Mix vs. A, A vs. B, and Mix vs. B, respectively ($p<0.05$, two-tailed t-test; Fig. 1D and I).

To identify odor frequency-discriminating cells, we performed statistical comparisons between the 2Hz and 20Hz conditions using the four time bins during the odor stimulation period: 0-0.5s, 0-1s, 0-1.5s, and 0-2s (where 0 denotes the start of odor stimulation; Fig. 1B). We observed that 41, 21, 29, and 41 out of 500 cells could significantly discriminate ($p<0.05$, two-tailed t-test) between 2Hz and 20Hz for odor A across the four time bins, respectively (Fig. 1E). For odor B, 59, 73, 99, and 101/500 cells showed significant discrimination (Fig. 1F), while for odor Mix, 22, 21, 38, and 34/500

cells (Fig. 1G) significantly discriminated between 2Hz and 20Hz odor stimuli across the four time bins, respectively. Overall, 4.4-11.8% of PYRs significantly discriminated between odor frequencies during the initial 500ms of stimulation.

To examine how accurately odor frequency could be identified from the spiking activity of populations of PCx neurons, we quantified the responses of all pyramidal neurons as vectors of 1s and 0s over the entire 2-second of odor stimulation period. This was accomplished by using a bin size of 20ms, based on whether a cell fired at least once within the specified time bin. We then trained and tested 1D CNN models on PYRs' activity from 2Hz and 20Hz odor trials (Fig. 2A). We observed that the models could achieve peak accuracies of 0.95 ± 0.016, 0.87 ± 0.032, and 0.73 ± 0.043 for odor A, B, and Mix, respectively, in discriminating 2Hz vs. 20Hz compared to their respective shuffled controls (mean ± SD). We also evaluated how decoding accuracy scaled with population size by training and testing CNNs on randomly selected subsets of PYRs (Fig. 2B-D). Each population size was evaluated over 144 independent iterations. We observed that the CNN models showed accuracies that increased monotonically with increasing numbers of cells. Peak classification accuracy varied with odor identity but consistently exceeded that of shuffled-label controls in all three odor conditions (Fig. 2B-D). To ensure our CNN models did not suffer from any intrinsic biasness, we trained and tested a set of models on the baseline activity (Fig. S5). We did not observe any significant difference in the models' accuracy compared to shuffle controls.

Next, we assessed each cell's contribution to the overall classification accuracy of the CNN model. To do this, we replaced the spiking activity of each cell (one at a time) during the odor stimulation period with that of its baseline period. Next, we estimated the difference in log-likelihood (intact minus perturbed, i.e., ΔLL) of the CNN model corresponding to each cellular perturbation, arranged in descending order (Fig. 2E-G). Larger differences indicated greater importance of the respective cell to frequency decoding. We observed subtle differences in ΔLL across the neuronal population. Furthermore, we tracked the significant odor frequency-discriminating cells on these traces and observed that they were located throughout the traces, which indicated that their true contribution to odor frequency decoding was distributed (Fig. 2E-G).

These results suggest that odor frequency discrimination in the PCx is a network phenomenon with a distributed role of importance among the cells. Overall, these experiments helped us observe that the CNN models could accurately decode responses between the 2Hz and 20Hz odor frequencies, surpassing the chance level (>0.5) for all three odor Mixtures. This suggests that the piriform cortex can discriminate between 2Hz and 20Hz odor frequencies.

Different synaptic connections differentially affect odor frequency discrimination

Next, we interrogated the role that each type of synaptic connection played in the PCx model in discriminating between the two odor frequencies 2Hz and 20Hz. To assess the role of specific circuit motifs, we virtually knocked out each synaptic connection type from the control network, one at a time. In these studies, the PCx knockout models were simulated 336 times over 6 seconds for the same odor stimuli (i.e., odor A, B, and Mix for 2Hz and 20Hz), and then the spiking activities of PYRs were examined in the same manner as before.

Eliminating feedforward or feedback inhibition enhanced odor frequency discrimination

To investigate the role of the inhibitory inputs onto the PYRs on odor frequency discrimination, we eliminated the synaptic connections from feedforward (FF) or feedback (FB) interneurons onto the PYRs in two different experiments (Fig. 3A, 4A). We built 1D-CNN models as before to test the binary classification accuracy between 2Hz and 20Hz odor frequency trials. Both knockout models yielded higher decoding accuracy compared to the control network. The peak accuracies achieved by the FF-PYR knockout models were A: 0.98 ± 0.006; B: 0.96 ± 0.011; and Mix: 0.87 ± 0.03 (Fig. 3B). The peak accuracies achieved by the FB-PYR knockout model were A: 0.99 ± 0.005; B: 0.97 ± 0.011; and Mix: 0.88 ± 0.02 (Fig. 4B). We estimated the number of significant odor frequency- and odor identity-discriminating cells as before for the initial 500ms of the odor stimulation period. We observed that in the case of the FF-PYR knockout model, 28, 46, and 38 (Fig. 3C) and 60, 140, and 46 (Fig. 3D) cells (Mix vs. A, A vs. B, and Mix vs. B, respectively) out of 500 cells showed significant odor identity discrimination (two-tailed t-test, $p<0.05$) for 2Hz and 20Hz stimuli, respectively. In the case of the FB-PYR knockout model, 28, 49, and 36 (Fig. 4C) and 64, 164, and 60 (Fig. 4D) cells

(Mix vs. A, A vs. B, and Mix vs. B, respectively) out of 500 showed significant odor identity discrimination (two-tailed t-test, $p<0.05$) for 2Hz and 20Hz stimuli, respectively.

For the case of FF-PYR, 108, 55, and 30 cells (A, B, and Mix, respectively) out of 500 cells showed significant frequency discrimination (Fig. 3E-G). For FB-PYR, 113 (A), 92 (B), and 25 (Mix) cells showed significant frequency discrimination (Fig. 4E-G). The percentage change in odor identity-encoding cells in the FF-PYR knockout model was 40% (Mix vs. A), 48.4% (A vs. B), and 5.5% (Mix vs. B) relative to the control group for 2Hz stimuli during the initial 500ms after odor stimulation (Fig. 3H). For 20Hz stimuli, the percentages were 42.8%, 45.8%, and 24.3% for the same odor pairs in the order provided (Fig. 3I). Similarly, for the FB-PYR knockout model, the percentage changes were 40%, 58.1%, and 0% for 2Hz stimuli (Fig. 4H) and 52.4%, 70.8%, and 62.2% for 20Hz stimuli (Fig. 4I) for odor pairs Mix vs. A, A vs. B, and Mix vs. B, respectively. The percentage changes in frequency-encoding cells relative to the control for the FF-PYR knockout model were 163.4%, -6.8%, and 36.4% for odor A, B, and Mix, respectively, during the first 500ms after odor stimulation. For the entire odor stimulation period, these percentage changes were 104.8%, 26.7%, and 2.9% for the same odor identities (Fig. 3J). Similarly, for the FB-PYR knockout model, these percentage changes were 175.6%, 56%, and 13.6% for odor A, B, and Mix, respectively, during the first 500ms after odor stimulation. For the entire odor stimulation period, these percentage changes were 173.2%, 107%, and 55.9% for the same odor identities (Fig. 4J). Notably, a greater proportion of cells significantly discriminated both odor identity and odor frequency in knockout models relative to the control (Fig. 3H–J, 4H–J). These observations indicate that eliminating either the FF or the FB inhibitory connections onto the PYRs results in enhanced frequency-encoding capacity of the PCx model.

Eliminating intra-inhibitory connections singularly had minimal effect on odor frequency discrimination

The PCx network contains a substantial amount of intra-inhibitory connections within feedforward (FF) as well as feedback (FB) interneurons (Stern et al., 2018b). To understand the role of these disinhibitory motifs in odor frequency discrimination, we eliminated the synaptic intra-connections

among FF or FB interneurons individually in two distinct knockout models (Fig. 5A, 6A). In both knockout scenarios, 1D CNN models successfully classified 2Hz vs. 20Hz stimuli. The peak accuracy for the FF-FF knockout model was A: 0.92 ± 0.016; B: 0.87 ± 0.023; and Mix: 0.7 ± 0.05, and that of the FB-FB knockout model was A: 0.93 ± 0.015; B: 0.87 ± 0.028; and Mix: 0.73 ± 0.04. The number of odor identity-encoding cells during the initial 500ms after stimulus onset for 2Hz stimuli in the FF-FF knockout model was 23, 32, and 25 out of 500 for Mix vs. A, A vs. B, and Mix vs. B, respectively (Fig. 5C). For 20Hz stimuli, the corresponding numbers were 24, 77, and 35 out of 500 for the same odor pairs (Fig. 5D). For the FB-FB knockout model, 26, 42, and 34 out of 500 cells (Fig. 6C) and 40, 75, and 41 out of 500 cells (Fig. 6D) showed significant odor identity discrimination for 2Hz and 20Hz stimuli, respectively (Mix vs. A, A vs. B, and Mix vs. B; two-tailed t-test, $p<0.05$). For the case of 2Hz vs. 20Hz odor frequency discrimination, 49, 45, and 23 out of 500 (A, B, and Mix, respectively) cells showed significant discrimination in the FF-FF knockout model (Fig. 5E-G). In the case of FB-FB knockout model, 56, 44, and 32 out of 500 (A, B, and Mix, respectively) cells showed significant odor frequency discrimination (Fig. 6E-G).

The percentage change in odor identity-encoding cells in the FF-FF knockout model relative to the control group was 15% (Mix vs. A), 3.2% (A vs. B), and –30.5% (Mix vs. B) for 2Hz stimuli during the initial 500ms after odor stimulation (Fig. 5H). For 20Hz stimuli, the corresponding percentages were –42.8%, –19.8%, and –5.4% for the same odor pairs (Fig. 5I). Similarly, for the FB-FB knockout model, the percentage changes were 30%, 35.5%, and –5.5% for 2Hz stimuli (Fig. 6H) and –4.7%, –21.8%, and 10.8% for 20Hz stimuli (Fig. 6I) for odor pairs Mix vs. A, A vs. B, and Mix vs. B, respectively. The percentage changes in frequency-encoding cells relative to the control for the FF-FF knockout model were 19.5%, –23.7%, and 4.5% for odors A, B, and Mix, respectively, during the first 500ms after odor stimulation. For the entire odor stimulation period, these percentage changes were 4.8%, –19.8%, and –29.41% for the same odor identities (Fig. 5J). Similarly, for the FB-FB knockout model, these percentage changes were 36.6%, –25.4%, and 45.4% for odors A, B, and Mix, respectively, during the first 500ms after odor stimulation. For the entire odor stimulation

period, these percentage changes were –2.4%, –29.7%, and –17.6% for the same odor identities (Fig. 6J).

No consistent trends were observed in the percentage change of odor identity- or frequency-encoding cells relative to the control in either FF-FF (Fig. 5H-J) or FB-FB (Fig. 6H-J) knockout models. Overall, the PCx network model's response for frequency encoding is quite robust to removal of inhibition within feedforward or feedback interneurons.

Eliminating excitatory or all intra-inhibitory recurrent connections impaired odor frequency discrimination

Finally, to investigate how removing recurrent inhibition onto both interneuron types affects frequency encoding in the PCx model, we developed a FF-FF and FB-FB knockout model (Fig. 7A). To investigate the same effect by removing recurrent excitation onto PYRs, we developed a PYR-PYR knockout model (Fig. 8A). 1D CNN decoding of odor frequency responses revealed a decline in classification accuracy for both knockout models across all size-matched populations of PYRs compared to the control group (Fig. 7B, 8B). The peak accuracies achieved by the FF-FF and FB-FB knockout model were A: 0.91 ± 0.02; B: 0.83 ± 0.029; and Mix: 0.67 ± 0.05 (Fig. 7B). The peak accuracies achieved by the PYR-PYR knockout model were A: 0.92 ± 0.02; B: 0.84 ± 0.03; and Mix: 0.69 ± 0.05 (Fig. 8B) compared to the control (A: 0.95 ± 0.016; B: 0.87 ± 0.032; and Mix: 0.73 ± 0.043). For the FF-FF and FB-FB knockout model 27, 33, and 24 cells (Fig. 7C) for 2Hz stimuli and 35, 48, and 33 cells (Fig. 7D) for 20Hz stimuli (Mix vs. A, A vs. B, and Mix vs. B, respectively) showed significant odor identity discrimination (two-tailed t-test, $p<0.05$) during the initial 500ms of the odor stimulation period.

Similarly, for the PYR-PYR knockout model, 21, 32, and 36 cells (Fig. 8C) for 2Hz stimuli and 49, 75, and 29 cells (Fig. 8D) for 20Hz stimuli (Mix vs. A, A vs. B, and Mix vs. B, respectively) showed significant odor identity discrimination (two-tailed t-test, $p<0.05$). For the 2Hz vs. 20Hz odor frequency discrimination, 40, 37, and 35 out of 500 (A, B, and Mix, respectively) cells showed significant discrimination in the FF-FF and FB-FB knockout model (Fig. 7E-G). For the PYR-PYR

knockout model, 57, 39, and 24 out of 500 (A, B, and Mix, respectively) cells showed significant discrimination of 2Hz vs. 20Hz (Fig. 8E-G).

The percentage change in odor identity-encoding cells in the FF-FF and FB-FB knockout model was 35% (Mix vs. A), 6.4% (A vs. B), and –33.3% (Mix vs. B) relative to the control group for 2Hz stimuli during the initial 500ms after odor stimulation (Fig. 7H). For 20Hz stimuli, the percentages were –16.7%, –50%, and –10.8% for the same odor pairs (Fig. 7I). Similarly, for the PYR-PYR knockout model, the percentage changes were 5%, 3.2%, and 0% for 2Hz stimuli (Fig. 8H) and 16.7%, –21.8%, and –21.7% for 20Hz stimuli (Fig. 8I) for odor pairs Mix vs. A, A vs. B, and Mix vs. B, respectively. The percentage changes in frequency-encoding cells relative to the control for the FF-FF and FB-FB knockout model were –2.4%, –37.3%, and 59% for odors A, B, and Mix, respectively, during the first 500ms after odor stimulation. For the entire odor stimulation period, these percentage changes were 14.6%, –36.6%, and 0% for the same odor identities (Fig. 7J). Similarly, for the PYR-PYR knockout model, these percentage changes were 39%, –33.9%, and 9.1% for odors A, B, and Mix, respectively, during the first 500ms after odor stimulation. For the entire odor stimulation period, these percentage changes were 26.8%, –30.7%, and 5.9% for the same odor identities (Fig. 8J).

Virtual knockout experiments demonstrated that eliminating direct inhibition onto PYRs enhanced frequency discrimination, whereas removing excitatory and all intra-inhibitory recurrent connections degraded decoding performance (see Table 3 for a comprehensive list of CNN models' peak accuracies).

Circuit motifs, not activity level, determine odor frequency representation

Synaptic modifications resulted in changes to the baseline firing rates of PYRs. Knocking out the direct inhibition onto the PYRs increased the baseline firing from 1.09 ± 0.726Hz (Control) to 1.32 ± 0.792Hz (FF-PYR knockout) and 2.08 ± 0.991Hz (FB-PYR knockout) (Fig. 9B). In contrast, knocking out recurrent synaptic connections among PYRs (PYR-PYR knockout) and both kinds of interneurons (FF-FF and FB-FB knockout) decreased the baseline firing rate to 0.992 ± 0.692Hz and

0.963 ± 0.683Hz, respectively. Because changes in frequency decoding accuracy correlated with baseline firing rates, we tested whether excitability alone could explain the decoding performance. To address this question, we modeled various control variants of the PCx network by systematically varying the spontaneous firing rates of pyramidal cells in the control network (Fig. 9A). The mean spontaneous activity of the PYRs in these variant models spans the entire range observed in the knockout models, with some variants exhibiting firing rates at the lower extreme and others at the upper extreme of the knockout distribution (Fig. 9B). A complete comparative list of baseline firing rates for each network model is provided in Table 4. We then performed odor frequency decoding using PYR population responses from control variants (Fig. 9C) and compared them with those obtained from the knockout models (Fig. 9D) across all odor conditions. The CNN models' performance using the activity data from the knockout models showed a correlation between enhancement or impairment of odor frequency classification and their mean population baseline firing rates relative to the control network across all odor conditions (Fig. 9D). In contrast, control variants showed either minimal differences in classification performance for odors A and B, or an entirely reversed correlation for odor Mix (Fig. 9C). This suggests that specific circuit motifs, and not just baseline excitability, are important for the PCx network to discriminate odor frequency.

Overall, we observed that the PCx network can discriminate 2Hz from 20Hz odor stimuli. The virtual knockout studies show that eliminating direct inhibition onto the PYRs increases the discrimination capacity of the network, while eliminating recurrent connections within the PCx (PYR-PYR or FF-FF and FB-FB) decreases the discrimination capacity. Furthermore, our analysis indicates that specific intracortical motifs, rather than merely changes in baseline excitability, are critical for shaping odor frequency representation.

Discussion

Mammalian and insect olfactory systems have long been recognized for their ability to encode chemical and physical properties of odor stimuli, such as odor identity, intensity, and concentration.

(Su et al., 2009). These systems also exhibit a remarkable capacity to encode the temporal structure of olfactory cues present in natural odor landscapes to guide behavioral decisions such as foraging, navigation, and locating or separating odor sources (Hopfield, 1991; Mylne and Mason, 1991; Murlis et al., 2003; Celani et al., 2014; Ackels et al., 2021; Marin et al., 2021b). A recent study in mice showed that mitral/tufted (M/T) cells in the OB can encode odor frequencies up to 20Hz (Dasgupta et al., 2022). However, whether cortical regions downstream of the OB, particularly the piriform cortex (PCx), participate in odor frequency encoding remains unclear. We investigated whether the PCx is capable of encoding odor stimulus frequencies. In our study, we used previously recorded *in vivo* activity from M/Ts in response to odor stimuli at 2Hz and 20Hz frequencies (Dasgupta et al., 2022) as input to a biophysically relevant PCx network model. We found that the PCx network model has the capacity to differentially encode the 2Hz and 20Hz odor stimulus frequency.

We then simulated several synaptic knockout variants of the PCx model to assess how frequency encoding is affected by circuit alterations. We found that removing either feedforward or feedback inhibition onto pyramidal neurons enhanced the convolutional neural network (CNN) model's ability to classify odor frequency response compared to the control PCx model. In contrast, knocking out either recurrent excitation onto PYRs or recurrent inhibition onto both feedforward (FF) and feedback (FB) interneurons resulted in slightly impaired classification performance. Notably, decoding performance remained comparable to the control when either FF–FF or FB–FB intra-inhibitory connections were removed.

Single cell vs. population coding

We sought to understand how individual PCx cells represent odor frequency. To study this, we initially used a cellular-level statistical approach based on the difference in average spiking rate during the odor stimulation period to classify cells into frequency-discriminating and non-discriminating types (two tailed t-test, $p<0.05$). PYRs that met this statistical threshold were classified as frequency-discriminating cells. Thus, according to this approach, only statistically significant cells contribute to frequency representation. This would result in a low-dimensional representation of a given parameter such as odor frequency in a systematically patterned network (Fusi et al., 2016).

However, prior studies indicate that multiple neurons often respond nonlinearly to represent a given stimulus parameter, which in turn helps the organism to perceive it (Rigotti et al., 2013; Kriegeskorte and Douglas, 2019; Saxena and Cunningham, 2019). Our data also show such overlap (Fig. 7C-G), with some cells encoding both odor identity and frequency. Overall, this approach is only partially predictive of a cell's importance for a given feature representation (Stefanini et al., 2020).

Therefore, we turned our attention to the population-level decoding of frequency information. As part of the network, activities of the individual neurons are correlated with each other at a specific time. Stefanini et al. (2020) experimentally demonstrated that due to this correlation, a decoder might assign larger weights to the weakly tuned or even untuned neurons when their activities are correlated with tuned neurons. Population decoders (pattern classifiers) using the average firing rate of neurons have been extensively used in different fields of neuroscience to predict decision boundaries from experimental outcomes. However, averaging spiking activity over long periods results in the loss of valuable information embedded in the temporal structure of the firing patterns of neuronal populations. To preserve this rich information, we employed a 1D Convolutional Neural Network (CNN) for odor frequency classification. This network utilizes the spiking activities of neurons across the entire stimulation period of 2 seconds. Each neuron's activity was represented as a binary vector of length 100 (100 × 20ms bins), where each component takes binary values (0/1) indicating whether the neuron spiked within a specific 20ms time bin. The 20ms bin size was selected to maximize the likelihood of capturing no more than one spike per bin. 1D CNN models, trained and tested on PYRs' neuronal activity, reliably distinguished odor stimuli presented at 2Hz vs. 20Hz (Fig. 2 B-D).

Using the trial-averaged (n=300) log-likelihood difference (ΔLL) for each neuron, we ranked them according to their importance/contribution to frequency decoding (Fig. 2E-G). The results indicate that decoding importance is distributed across a substantial portion of the PYR population. Overlaying the significant cells (estimated using the cellular level statistical approach) on these ranking plots showed that the important neurons having the highest contribution at the population level are highly heterogeneous in their frequency tuning.

In summary, our results suggest that almost every active neuron contributes to frequency decoding, which is a hallmark of distributed neural code.

The encoding role of circuit motifs

Cellular and circuit elements, essentially interneurons, have been observed to play key roles in modifying network outputs in other brain areas, such as the hippocampus (Dasgupta and Sikdar, 2015, 2019). Different circuit motifs differentially shape PCx responses (Stern et al., 2018b). Several experiments have elucidated the role of inhibitory and recurrent circuitry in encoding temporally dynamic structure of odor stimuli in the olfactory circuit (Nagel, Hong and Wilson, 2015; Burton, 2017; Bolding et al., 2020, Dasgupta et al., 2022). These effects can emerge through both spiking patterns and subthreshold membrane potential dynamics. Usually, active neurons have been observed to contribute to stimulus encoding. However, stimulus-evoked deviations from baseline activity are critical for encoding. It has been proved that the importance of a cell in an encoding population is strongly correlated with its average response property (Stefanini et al., 2020). A neuron's average response is shaped by the balance of excitatory and inhibitory inputs it receives. We tested this by altering the noise current to match the baseline firing of the PYR population to that for the different knockout cases (Fig. 9). However, such a general modulation in baseline activity could not achieve a similar decoding accuracy as the knockout cases. However, such a general modulation in baseline activity could not achieve a similar decoding accuracy as the knock-out cases. This indicated that specific circuit motifs that are intertwined with the pyramidal cells of the piriform cortex both spatially and temporally sculpt the output response and hence are necessary for the specific decoding modulation. Experimental and theoretical studies will be required in the future to understand how each of these circuit motifs are able to modulate the decoding performance of the PCx network.

Thus, our findings from various knockout models suggest that the odor frequency representation in the piriform cortex is dependent on specific circuit motifs.

Limitations of our model circuit

The current model simplifies PCx circuitry by not differentiating among various neuronal subtypes. We did not distinguish different subclasses of principal neurons (e.g. semilunar cells vs. superficial pyramidal cells), feedforward interneurons (e.g., horizontal cells vs. neurogliaform cells) and feedback interneurons (e.g. regular-spiking multipolar vs. fast-spiking multipolar vs. bitufted vs. neurogliaform cells). Semilunar and superficial pyramidal neurons are functionally distinct subtypes owing to their specialization in afferent and intracortical processing, respectively (Suzuki and Bekkers, 2011). Additionally, distinct interneuron subtypes contribute to layer-specific phasic inhibition of layer II principal neurons and hence play specific roles in cortical odor processing (Suzuki and Bekkers, 2010). In our model circuit we did not incorporate the centrifugal/feedback projections from the PCx back to the OB. These cortical feedback projections provide strongly normalized activity over diverse olfactory stimuli, which can be combined with the highly unbalanced activities of OSNs to influence M/T responses (Zak et al., 2024). The range of odor stimuli in our simulations was also limited in terms of Mixture complexity, concentration, and frequency range. It would be intriguing to investigate the impact of these parameters on the frequency encoding capacity of the PCx. For instance, throughout our results, we observed poor decoding of odor frequency responses for odor Mix compared to odor A and B.

Overall, our results suggest that the PCx network has the capacity to encode odor frequencies associated with naturalistic odor stimuli. This will be interesting to validate experimentally as temporal dynamics in sensory stimuli have been thought to be an important route of information transfer to our brain.

Author Contributions

DD conceived the project. DD and AK designed simulation experiments. AK performed simulation experiments and analyzed data. DD, AK, AM, OC, and MJ designed experiments for 1D CNN modelling. OC, MJ, and AK performed 1D-CNN modelling and analyzed data. AK and DD wrote the manuscript and edited it with input from all authors.

627

References

Ackels T, Erskine A, Dasgupta D, Marin AC, Warner TPA, Tootoonian S, Fukunaga I, Harris JJ, Schaefer AT (2021) Fast odour dynamics are encoded in the olfactory system and guide behaviour. Nature 2021 593:7860 593:558–563 Available at: https://www.nature.com/articles/s41586-021-03514-2 [Accessed January 23, 2025].

Bathellier B, Margrie TW, Larkum ME (2009) Properties of Piriform Cortex Pyramidal Cell Dendrites: Implications for Olfactory Circuit Design. Journal of Neuroscience 29:12641–12652 Available at: https://www.jneurosci.org/content/29/40/12641 [Accessed January 28, 2025].

Bekkers JM, Suzuki N (2013) Neurons and circuits for odor processing in the piriform cortex. Trends Neurosci 36:429–438 Available at: http://www.cell.com/article/S0166223613000660/fulltext [Accessed January 31, 2025].

Bolding KA, Franks KM (2017) Complementary codes for odor identity and intensity in olfactory cortex. Elife 6.

Bolding KA, Nagappan S, Han BX, Wang F, Franks KM (2020) Recurrent circuitry is required to stabilize piriform cortex odor representations across brain states. Elife 9:1–23.

Burton SD (2017) Inhibitory circuits of the mammalian main olfactory bulb. Available at: www.jn.org [Accessed May 21, 2025].

Caprio J, Derby CD (2008) Aquatic Animal Models in the Study of Chemoreception. The Senses: A Comprehensive Reference 4:97–133.

Carnevale T, Hines M (2005) The NEURON Book. Available at: www.cambridge.org [Accessed July 8, 2025].

Celani A, Villermaux E, Vergassola M (2014) Odor landscapes in turbulent environments. Phys Rev X 4:041015 Available at: https://journals.aps.org/prx/abstract/10.1103/PhysRevX.4.041015 [Accessed February 24, 2025].

Crimaldi J, Lei H, Schaefer A, Schmuker M, Smith BH, True AC, Verhagen J V., Victor JD (2022) Active sensing in a dynamic olfactory world. J Comput Neurosci 50:1–6 Available at: https://link.springer.com/article/10.1007/s10827-021-00798-1 [Accessed February 24, 2025].

Dasgupta D, Sikdar SK (2015) Calcium permeable AMPA receptor-dependent long lasting plasticity of intrinsic excitability in fast spiking interneurons of the dentate gyrus decreases inhibition in the granule cell layer. Hippocampus 25:269–285 Available at: https://onlinelibrary.wiley.com/doi/full/10.1002/hipo.22371 [Accessed July 11, 2025].

Dasgupta D, Sikdar SK (2019) Heterogeneous network dynamics in an excitatory-inhibitory network model by distinct intrinsic mechanisms in the fast spiking interneurons. Brain Res 1714:27–44 Available at: https://pubmed.ncbi.nlm.nih.gov/30771318/ [Accessed July 11, 2025].

Dasgupta D, Warner TPA, Erskine A, Schaefer AT (2022) Coupling of Mouse Olfactory Bulb Projection Neurons to Fluctuating Odor Pulses. Journal of Neuroscience 42:4278–4296 Available at: https://www.jneurosci.org/content/42/21/4278 [Accessed January 23, 2025].

de Almeida L, Idiart M, Linster C (2013) A model of cholinergic modulation in olfactory bulb and piriform cortex. J Neurophysiol 109:1360–1377 Available at: https://journals.physiology.org/doi/10.1152/jn.00577.2012 [Accessed January 23, 2025].

Duchamp-Viret P, Chaput MA, Duchamp A (1999) Odor Response Properties of Rat Olfactory Receptor Neurons. Science (1979) 284:2171–2179 Available at: https://www.science.org/doi/10.1126/science.284.5423.2171 [Accessed July 1, 2025].

Fischler-Ruiz W, Clark DG, Joshi NR, Devi-Chou V, Kitch L, Schnitzer M, Abbott LF, Axel R (2021) Olfactory landmarks and path integration converge to form a cognitive spatial map. Neuron 109:4036-4049.e5 Available at: https://pubmed.ncbi.nlm.nih.gov/34710366/ [Accessed July 8, 2025].

Franks KM, Russo MJ, Sosulski DL, Mulligan AA, Siegelbaum SA, Axel R (2011a) Recurrent Circuitry Dynamically Shapes the Activation of Piriform Cortex. Neuron 72:49–56.

Franks KM, Russo MJ, Sosulski DL, Mulligan AA, Siegelbaum SA, Axel R (2011b) Recurrent circuitry dynamically shapes the activation of piriform cortex. Neuron 72:49 Available at: https://pmc.ncbi.nlm.nih.gov/articles/PMC3219421/ [Accessed June 8, 2025].

Fusi S, Miller EK, Rigotti M (2016) Why neurons mix: high dimensionality for higher cognition. Curr Opin Neurobiol 37:66–74 Available at: https://www.sciencedirect.com/science/article/pii/S0959438816000118 [Accessed May 20, 2025].

Gumaste A, Baker KL, Izydorczak M, True AC, Vasan G, Crimaldi JP, Verhagen J (2024) Behavioral discrimination and olfactory bulb encoding of odor plume intermittency. Elife 12.

Hopfield JJ (1991) Olfactory computation and object perception. Proceedings of the National Academy of Sciences 88:6462–6466 Available at: https://www.pnas.org/doi/abs/10.1073/pnas.88.15.6462 [Accessed January 30, 2025].

Huston SJ, Stopfer M, Cassenaer S, Aldworth ZN, Laurent G (2015) Neural Encoding of Odors during Active Sampling and in Turbulent Plumes. Neuron 88:403–418.

Ikeda K, Suzuki N, Bekkers JM (2018) Sodium and potassium conductances in principal neurons of the mouse piriform cortex: a quantitative description. J Physiol 596:5397–5414 Available at: https://onlinelibrary.wiley.com/doi/full/10.1113/JP275824 [Accessed January 28, 2025].

Isaacson JS (2010) Odor representations in mammalian cortical circuits. Curr Opin Neurobiol 20:328–331.

Koehl MAR (2006) The Fluid Mechanics of Arthropod Sniffing in Turbulent Odor Plumes. Chem Senses 31:93–105 Available at: https://dx.doi.org/10.1093/chemse/bjj009 [Accessed February 24, 2025].

Kriegeskorte N, Douglas PK (2019) Interpreting encoding and decoding models. Curr Opin Neurobiol 55:167–179 Available at:

https://www.sciencedirect.com/science/article/pii/S0959438818301004 [Accessed May 20, 2025].

Laurent G, Wehr M, Davidowitz H (1996) Temporal Representations of Odors in an Olfactory Network. The Journal of Neuroscience 16:3837 Available at: https://pmc.ncbi.nlm.nih.gov/articles/PMC6578619/ [Accessed May 10, 2025].

Lewis SM, Suarez LM, Rigolli N, Franks KM, Steinmetz NA, Gire DH (2024) The spiking output of the mouse olfactory bulb encodes large-scale temporal features of natural odor environments. bioRxiv:2024.03.01.582978 Available at: https://www.biorxiv.org/content/10.1101/2024.03.01.582978v1 [Accessed July 8, 2025].

Linster C, Menon A V., Singh CY, Wilson DA (2009) Odor-specific habituation arises from interaction of afferent synaptic adaptation and intrinsic synaptic potentiation in olfactory cortex. Learning & Memory 16:452–459 Available at: http://learnmem.cshlp.org/content/16/7/452.full [Accessed January 21, 2025].

Lucas P, Lei H, Olsson SB, Pannunzi M, Nowotny T (2019) Odor Stimuli: Not Just Chemical Identity. Front Physiol 10:1428 Available at: https://pmc.ncbi.nlm.nih.gov/articles/PMC6890726/ [Accessed February 24, 2025].

Marin AC, Schaefer AT, Ackels T (2021a) Spatial information from the odour environment in mammalian olfaction. Cell Tissue Res 383:473 Available at: https://pmc.ncbi.nlm.nih.gov/articles/PMC7872987/ [Accessed May 10, 2025].

Marin AC, Schaefer AT, Ackels T (2021b) Spatial information from the odour environment in mammalian olfaction. Cell Tissue Res 383:473–483 Available at: https://pubmed.ncbi.nlm.nih.gov/33515294/ [Accessed February 24, 2025].

Migliore M, Hoffman DA, Magee JC, Johnston D (1999) Role of an A-type K+ conductance in the back-propagation of action potentials in the dendrites of hippocampal pyramidal neurons. J Comput Neurosci 7:5–15 Available at: https://modeldb.science/2796 [Accessed January 27, 2025].

Mori K, Sakano H (2021) Olfactory Circuitry and Behavioral Decisions. Annu Rev Physiol 83:231–256 Available at: https://www.annualreviews.org/content/journals/10.1146/annurev-physiol-031820-092824 [Accessed July 8, 2025].

Murlis J, Elkinton J, entomology RC-A review of, 1992 undefined (2003) Odor plumes and how insects use them. researchgate.netJ Murlis, JS Elkinton, RT CardeAnnual review of entomology, 1992•researchgate.net 37:505–537 Available at: https://www.researchgate.net/profile/Ring-Carde/publication/234150143_Odor_Plumes_and_How_Insects_Use_Them/links/00b7d52bcdfc033642000000/Odor-Plumes-and-How-Insects-Use-Them.pdf [Accessed January 30, 2025].

Mylne KR, Mason PJ (1991) Concentration fluctuation measurements in a dispersing plume at a range of up to 1000 m. Quarterly Journal of the Royal Meteorological Society 117:177–206 Available at: https://onlinelibrary.wiley.com/doi/full/10.1002/qj.49711749709 [Accessed January 30, 2025].

Nagappan S, Franks KM (2021) Parallel processing by distinct classes of principal neurons in the olfactory cortex. Elife 10.

Nagel KI, Hong EJ, Wilson RI (2015) Synaptic and circuit mechanisms promoting broadband transmission of olfactory stimulus dynamics. Nat Neurosci 18:56–65 Available at: https://pubmed.ncbi.nlm.nih.gov/25485755/ [Accessed May 18, 2025].

Poo C, Isaacson JS (2009) Odor Representations in Olfactory Cortex: "Sparse" Coding, Global Inhibition, and Oscillations. Neuron 62:850–861 Available at: http://www.cell.com/article/S0896627309003973/fulltext [Accessed February 13, 2025].

Rigotti M, Barak O, Warden MR, Wang XJ, Daw ND, Miller EK, Fusi S (2013) The importance of mixed selectivity in complex cognitive tasks. Nature 497:585–590 Available at: https://www.nature.com/articles/nature12160 [Accessed May 20, 2025].

Saxena S, Cunningham JP (2019) Towards the neural population doctrine. Curr Opin Neurobiol 55:103–111 Available at: https://www.sciencedirect.com/science/article/pii/S0959438818300990 [Accessed May 20, 2025].

Shralman BI, Siggia ED (2000) Scalar turbulence. Nature 2000 405:6787 405:639–646 Available at: https://www.nature.com/articles/35015000 [Accessed February 24, 2025].

Stefanini F, Kushnir L, Jimenez JC, Jennings JH, Woods NI, Stuber GD, Kheirbek MA, Hen R, Fusi S (2020) A Distributed Neural Code in the Dentate Gyrus and in CA1. Neuron 107:703-716.e4 Available at: https://www.sciencedirect.com/science/article/pii/S0896627320303913 [Accessed May 19, 2025].

Stern M, Bolding KA, Abbott LF, Franks KM (2018a) A transformation from temporal to ensemble coding in a model of piriform cortex. Elife 7.

Stern M, Bolding KA, Abbott LF, Franks KM (2018b) A transformation from temporal to ensemble coding in a model of piriform cortex. Elife 7.

Stokes CCA, Isaacson JS (2010a) From Dendrite to Soma: Dynamic Routing of Inhibition by Complementary Interneuron Microcircuits in Olfactory Cortex. Neuron 67:452–465 Available at: http://www.cell.com/article/S0896627310005131/fulltext [Accessed January 21, 2025].

Stokes CCA, Isaacson JS (2010b) From Dendrite to Soma: Dynamic Routing of Inhibition by Complementary Interneuron Microcircuits in Olfactory Cortex. Neuron 67:452–465.

Su CY, Menuz K, Carlson JR (2009) Olfactory Perception: Receptors, Cells, and Circuits. Cell 139:45–59 Available at: https://www.cell.com/action/showFullText?pii=S0092867409011751 [Accessed May 18, 2025].

Suzuki N, Bekkers JM (2010) Distinctive Classes of GABAergic Interneurons Provide Layer-Specific Phasic Inhibition in the Anterior Piriform Cortex.

Suzuki N, Bekkers JM (2011) Two Layers of Synaptic Processing by Principal Neurons in Piriform Cortex. Journal of Neuroscience 31:2156–2166 Available at: https://www.jneurosci.org/content/31/6/2156 [Accessed June 4, 2025].

Suzuki N, cortex JB-C, 2010 undefined (2010) Distinctive classes of GABAergic interneurons provide layer-specific phasic inhibition in the anterior piriform cortex. academic.oup.comN

Suzuki, JM BekkersCerebral cortex, 2010•academic.oup.com Available at: https://academic.oup.com/cercor/article-abstract/20/12/2971/367693 [Accessed January 28, 2025].

Szyszka P (2005) Odor coding and neural plasticity in the mushroom body of the honeybee. Available at: https://refubium.fu-berlin.de/handle/fub188/12883 [Accessed May 10, 2025].

Vickers NJ (2000) Mechanisms of animal navigation in odor plumes. https://doi.org/102307/1542524 198:203–212 Available at: https://www.journals.uchicago.edu/doi/10.2307/1542524 [Accessed January 30, 2025].

Vickers NJ, Baker TC (1994) Reiterative responses to single strands of odor promote sustained upwind flight and odor source location by moths. Proceedings of the National Academy of Sciences 91:5756–5760 Available at: https://www.pnas.org/doi/abs/10.1073/pnas.91.13.5756 [Accessed February 24, 2025].

Vickers NJ, Christensen TA, Baker TC, Hildebrand JG (2001) Odour-plume dynamics influence the brain's olfactory code. Nature 410:466–470 Available at: https://pubmed.ncbi.nlm.nih.gov/11260713/ [Accessed February 24, 2025].

Wang XJ, Buzsáki G (1996) Gamma Oscillation by Synaptic Inhibition in a Hippocampal Interneuronal Network Model. Journal of Neuroscience 16:6402–6413 Available at: https://www.jneurosci.org/content/16/20/6402 [Accessed January 27, 2025].

Wu Y, Chen K, Xing C, Huang M, Zhao K, Zhou W (2024) Human olfactory perception embeds fine temporal resolution within a single sniff. Nature Human Behaviour 2024 8:11 8:2168–2178 Available at: https://www.nature.com/articles/s41562-024-01984-8 [Accessed July 1, 2025].

Zak JD, Reddy G, Konanur V, Murthy VN (2024) Distinct information conveyed to the olfactory bulb by feedforward input from the nose and feedback from the cortex. Nature Communications 2024 15:1 15:1–16 Available at: https://www.nature.com/articles/s41467-024-47366-6 [Accessed February 13, 2025].

Legends

Figure 1. PCx neurons discriminate between odor identities and frequencies. **A,** Schematic of the piriform cortex (PCx) network model. **B,** Representative voltage traces from three model pyramidal neurons (PYRs) in response to the three odor mixtures A, B, and Mix presented at 2Hz (blue) and 20Hz (red) frequency. **C-D,** Heatmaps of the p-values obtained from pairwise odor identity discrimination by PYRs, based on the initial 500ms of odor stimulation at 2Hz and 20Hz. Each row corresponds to a single cell, and the color indicates the p-value (two tailed t-test) for each odor pair comparison (see Materials and Methods for estimating p-values). **E-G,** Heatmaps of p-values for odor frequency discrimination (2Hz vs. 20Hz) by PYRs, estimated from the initial 0.5s, 1s, 1.5s and 2s of odor stimulation time period. Individual rows have a similar meaning as in C and D. **H,** 20/500, 31/500, and 36/500 PYRs and 42/500, 96/500, and 37/500 PYRs in **I** showed significant pairwise odor identity discrimination at 2Hz and 20Hz respectively ($p<0.05$, two-tailed t-test) during the first 500ms of odor stimulation. **J,** 41/500, 59/500, and 22/500 PYRs and 41/500, 101/500, and 34/500 PYRs showed significant discrimination between 2Hz and 20Hz ($p<0.05$, two-tailed t-test) based on the first 500ms (hollow bars), or the entire 2s odor stimulation period (colored bars).

Figure 2. 1D-CNN models demonstrate that PCx network activity can decode odor frequency. **A,** Schematic showing the preparation of datasets using spike times of PYRs during the entire 2s odor stimulation period, and the configuration of 1D convolutional neural network (CNN) for frequency classification. **B-D,** Average classification accuracy as a function of PYR population size. Solid lines represents the mean, and the shaded region represents the standard deviation (n = 144). **E-G,** Plots showing the difference in log likelihood values (ΔLL) between intact and perturbed test set for each neuron in the descending order of their importance for frequency decoding. In the perturbed test set, a neuron's spiking activity was replaced by its baseline activity. Statistically significant frequency-encoding cells (Fig. 1J), are marked in blue. Solid lines represents the mean, and the shaded region represents the standard deviation (n = 300).

Figure 3. Removing feedforward inhibition onto PYRs increases the frequency encoding capacity of PCx. **A,** Schematic of a PCx knockout model in which synaptic connections from feedforward

interneurons (FFINs) onto pyramidal neurons (PYRs) were removed. Knocked-out synaptic connections are indicated by hollow triangles in the circuit schematic. **B,** Average frequency classification accuracy as a function of PYR population size, using outputs from the control (blue) and knockout (red) network models. Solid lines represents the mean, and the shaded region represents the standard deviation (n = 144). **C-D,** Heatmaps of p-values from pairwise odor identity discrimination by PYRs, based on the initial 500ms of odor stimulation at 2Hz and 20Hz. Row meanings are as in Fig. 1C-D. **E-G,** Heatmaps of p-values for frequency discrimination (2Hz vs. 20Hz) by PYRs during the initial 500ms of odor stimulation. Individual rows have the same meaning as in Fig. 1E-G. **H,** Percent change in the number of PYRs exhibiting significant odor identity discrimination at 2Hz relative to control: 40.0%, 48.4%, and 5.4%; and at 20Hz (**I**): 42.8%, 45.8%, and 24.3%. **J,** Percent change in the number of PYRs (relative to control) showing significant frequency discrimination ($p < 0.05$, two-tailed t-test), based on the first 500ms (hollow bars): 163.4%, –6.8%, and 36.4%; and over the full 2s odor stimulation period (colored bars): 104.8%, 26.7%, and 2.9%.

Figure 4. Removing feedback inhibition onto PYRs increases the frequency encoding capacity of PCx. **A,** Schematic of the PCx knockout model in which synaptic connections from feedback interneurons (FBINs) onto pyramidal neurons (PYRs) were removed. The knocked-out synaptic connections are indicated by hollow triangles in the circuit schematic. **B,** Average frequency classification accuracy as a function of PYR population size, using outputs from the control (blue) and knockout (red) network models. Solid lines represents the mean, and the shaded region represents the standard deviation (n = 144). **C-D,** Heatmaps of p-values from pairwise odor identity discrimination by PYRs, based on the initial 500ms of odor stimulation at 2Hz and 20Hz. Rows are as defined in Fig. 1C-D. **E-G,** Heatmaps of p-values for frequency discrimination (2Hz vs. 20Hz) by PYRs during the initial 500ms of odor stimulation. Row meanings are as in Fig. 1E-G. **H,** Percent change (relative to control) in the number of PYRs showing significant pairwise odor identity discrimination at 2Hz: 40.0%, 58.1%, and 0.0%; and at 20Hz (**I**): 52.4%, 70.8%, and 62.2%. **J,** Percent change in the number of PYRs (relative to control) showing significant frequency discrimination ($p < 0.05$, two-tailed t-

test), based on the first 500ms (hollow bars): 175.6%, 56.0%, and 13.6%; and over the entire 2s odor stimulation period (colored bars): 173.2%, 107.0%, and 55.9%.

Figure 5. Frequency encoding capacity of the PCx network model decreases slightly due to the removal of recurrent inhibition within FFINs. **A,** Schematic of PCx knockout model which synaptic connections among feedforward interneurons (FFINs) were removed. Knocked-out synaptic connections are indicated by hollow triangles in the circuit schematic. **B,** Average frequency classification accuracy as a function of PYR population size, using outputs from the control (blue) and knockout (red) network models. Solid lines represents the mean, and the shaded region represents the standard deviation (n = 144). **C-D,** Heatmaps of p-values from pairwise odor identity discrimination by PYRs, based on the initial 500ms of odor stimulation at 2Hz and 20Hz. The rows have the same meanings as in Fig. 1C-D. **E-G,** Heatmaps of p-values for frequency discrimination (2Hz vs. 20Hz) by PYRs during the initial 500ms of odor stimulation. Row meanings are as in Fig. 1E-G. **H,** Percent change (relative to control) in the number of PYRs exhibiting significant pairwise odor identity discrimination at 2Hz: 15.0%, 3.2%, and –30.5%; and at 20Hz (**I**): –42.8%, –19.8%, and –5.4%. **J,** Percent change in the number of PYRs (relative to control) showing significant frequency discrimination ($p < 0.05$, two-tailed t-test), based on the first 500ms (hollow bars): 19.5%, –23.7%, and 4.5%; and over the full 2s odor stimulation period (colored bars): 4.8%, –19.8%, and –29.4%.

Figure 6. Frequency encoding capacity of PCx network model is robust to the removal of recurrent inhibition within FBINs. **A,** Schematic of the PCx knockout model in which synaptic connections among feedback interneurons (FBINs) were removed. Knocked-out synaptic connections are indicated by hollow triangles in the circuit schematic. **B,** Average frequency classification accuracy as a function of PYR population size, using outputs from the control (blue) and knockout (red) network models. Solid lines represents the mean, and the shaded region represents the standard deviation (n = 144). **C-D,** Heatmaps of p-values from pairwise odor identity discrimination by PYRs, based on the first 500ms of odor stimulation at 2Hz and 20Hz. The rows have the same meaning as in Fig. 1C-D. **E-G,** Heatmaps of p-values obtained from PYRs' response for 2Hz vs. 20Hz odor frequencies in the initial 500ms of odor stimulation. Individual rows have the same meaning as in Fig. 1E-G. **H,** Percent

change (relative to control) in the number of PYRs showing significant pairwise odor identity discrimination at 2Hz: 30.0%, 35.5%, and –5.5%; and at 20Hz (**I**): –4.7%, –21.8%, and 10.8%. **J,** Percent change in the number of PYRs (relative to control) showing significant frequency discrimination ($p < 0.05$, two-tailed t-test), based on the first 500ms (hollow bars): 36.6%, –25.4%, and 45.4%; and over the full 2s odor stimulation period (colored bars): –2.4%, –29.7%, and –17.6%.

Figure 7. Impairment of frequency encoding capacity of PCx network model after removal of recurrent inhibition within both FFINs and FBINs. **A,** Schematic of the PCx knockout model in which synaptic connections among both feedforward interneurons (FFINs) and feedback interneurons (FBINs) were removed. Knocked-out synaptic connections are indicated by hollow triangles in the circuit schematic. **B,** Average frequency classification accuracy as a function of PYR population size, using outputs from the control (blue) and knockout (red) network models. Solid lines represents the mean, and the shaded region represents the standard deviation (n = 144). **C-D,** Heatmaps of p-values from pairwise odor identity discrimination by PYRs, based on the first 500ms of odor stimulation at 2Hz and 20Hz. The rows have the same meaning as in Fig. 1C-D. **E-G,** Heatmaps of p-values obtained from PYRs' response for 2Hz vs. 20Hz odor frequencies in the initial 500ms of odor stimulation. Individual rows have the same meaning as in Fig. 1E-G. **H,** Percent change (relative to control) in the number of PYRs showing significant pairwise odor identity discrimination at 2Hz: 35.0%, 6.4%, and –33.3%; and at 20Hz (**I**): –16.7%, –50.0%, and –10.8%. **J**, Percent change in the number of PYRs (relative to control) showing significant frequency discrimination ($p < 0.05$, two-tailed t-test), based on the first 500ms (hollow bars): –2.4%, –37.3%, and 59.0%; and over the full 2s odor stimulation period (colored bars): 14.6%, –36.6%, and 0.0%.

Figure 8. Decline in frequency encoding capacity of PCx network model following removal of recurrent excitation onto PYRs. **A,** Schematic of the PCx knockout model in which recurrent synaptic connections among pyramidal neuons (PYRs) were removed. Knocked-out synaptic connections are indicated by hollow triangles in the circuit schematic. **B,** Average frequency classification accuracy as a function of PYR population size, using outputs from the control (blue) and knockout (red) network models. Solid lines represents the mean, and the shaded region represents the standard deviation (n =

144). **C-D,** Heatmaps of p-values from pairwise odor identity discrimination by PYRs, based on the first 500ms of odor stimulation at 2Hz and 20Hz. The rows have the same meaning as in Fig. 1C-D. **E-G,** Heatmaps of p-values obtained from PYRs' response for 2Hz vs. 20Hz odor frequencies in the initial 500ms of odor stimulation. Individual rows have the same meaning as in Fig. 1E-G. **H,** Percent change (relative to control) in the number of PYRs showing significant pairwise odor identity discrimination at 2Hz: 5.0%, 3.2%, and 0.0%; and at 20Hz (**I**): 16.7%, –21.8%, and –21.7%. **J**, Percent change in the number of PYRs (relative to control) showing significant frequency discrimination ($p < 0.05$, two-tailed t-test), based on the first 500ms (hollow bars): 39.0%, –33.9%, and 9.1%; and over the full 2s odor stimulation period (colored bars): 26.8%, –30.7%, and 5.9%.

Figure 9. Circuit motifs, not activity level, determine odor frequency representation in the PCx. **A,** Example voltage traces from PYRs in control and variant networks (Control '-3' to Control '+3'), showing baseline activity levels modulated by varying the baseline noise, resulting in firing rates ranging from 0.635 ± 0.56 Hz to 2.98 ± 1.14 Hz. **B,** Baseline firing rates of the PYR population across control variants (left panel) and knockout models (right panel). Bar heights represent mean firing rates, and error bars indicate standard deviations (n = 336 trials). **C,** Odor frequency decoding accuracy as a function of PYR population size for control variants across three odor conditions (Odor A, Odor B, and Odor Mix). Solid lines represents the mean, and the shaded region represents the standard deviation (n = 144). **D,** Odor frequency decoding accuracy as a function of PYR population size for knockout models across the same three odor conditions. Solid lines and shaded regions are defined as in **C** (n = 144).

Figure S1. Biophysical model of piriform cortex neurons. **A,** Schematic representation of a pyramidal neuron (PYR) model, consisting of a somatic compartment and five dendritic sections arranged from bottom to top. The model incorporates sodium (Na^+), delayed rectifier potassium (K^+), and leak ion channels, with their respective maximal conductance (gmax) and reversal potentials (E) indicated. **B-C,** Schematics of single compartment models of a feedforward interneuron (FFIN, **B**) and a feedback

interneuron (FBIN, **C**), with the respective peak conductance and reversal potentials of the Na^+, K^+, and leak ion channels.

Figure S2. Electrophysiological properties of a pyramidal neuron model. **A,** Step current injections vs. resulting voltage responses from soma and five dendrites (Dend_sec1 to Dend_sec5). **B,** Measured steady-state voltage changes in the soma and dendritic sections as a function of injected current. The slope of linear regression for each trace gives the input resistance of the corresponding compartment. **C,** Action potentials evoked at suprathreshold current in each of the soma and dendritic sections. **D,** This panel shows the mean spontaneous firing frequency (means ± SD) recorded from each of the sections across trials (n = 100). **E,** Plot of firing frequency vs. current step amplitude across all compartments. **F,** Example voltage vs. time traces of spontaneous activity recorded from soma and each dendritic section.

Figure S3. Electrophysiological properties of a feedforward interneuron model. **A,** Voltage responses recorded from the soma in response to step current injections. **B,** Left, Step current injections in the soma. Middle: Corresponding voltage responses recorded from the soma. Right, Plot of voltage change vs. injected current and its linear regression analysis to obtain the corresponding input resistance. **C,** Plot of an action potential recorded from the soma (I) and the corresponding phase plot (II) **D,** Plot of firing frequency vs. current step amplitude **E,** Example voltage traces of spontaneous activity recorded from the soma. **F,** Average spontaneous firing frequency (means ± SD) recorded across trials (n = 100).

Figure S4. Electrophysiological properties of a feedback interneuron model. **A,** Voltage responses recorded from the soma in response to step current injections. **B,** Left, Step current injections in the soma. Middle: Corresponding voltage responses recorded from the soma. Right, Plot of voltage change vs. injected current and its linear regression analysis to obtain the corresponding input resistance. **C,** Plot of an action potential recorded from the soma (I) and the corresponding phase plot (II) **D,** Plot of firing frequency vs. current step amplitude. **E,** Example voltage traces of spontaneous activity recorded from the soma. **F,** Average spontaneous firing frequency (means ± SD) recorded across trials (n = 100).

Figure S5. Decoding odor frequency from baseline activity under various synaptic knockout conditions. Bar plots show CNN classification accuracy for discriminating 2Hz vs. 20Hz odor conditions using only pre-stimulus/baseline (0–2s) firing activity of all pyramidal neurons, alongside corresponding shuffle controls. Each panel represents a distinct synaptic disconnection: (**A**) Control, (**B**) FF–PYR, (**C**) FB–PYR, (**D**) FF–FF, (**E**) FB–FB, (**F**) FF–FF and FB–FB, and (**G**) PYR–PYR. Accuracy is reported across three odor conditions (A, B, and Mix), with each condition evaluated over 144 iterations using a random 60%/40% train-test split. Classification performance using activity was statistically compared to chance-level decoding (shuffle condition) using a two-tailed t-test ($p < 0.05$).

Table 1. Morphological and biophysical parameters of the modeled cells of PCx.

Table 2. Model parameters

Table 3. Peak accuracies

Table 4. PYRs baseline firing rate (Hz)

Figure 1

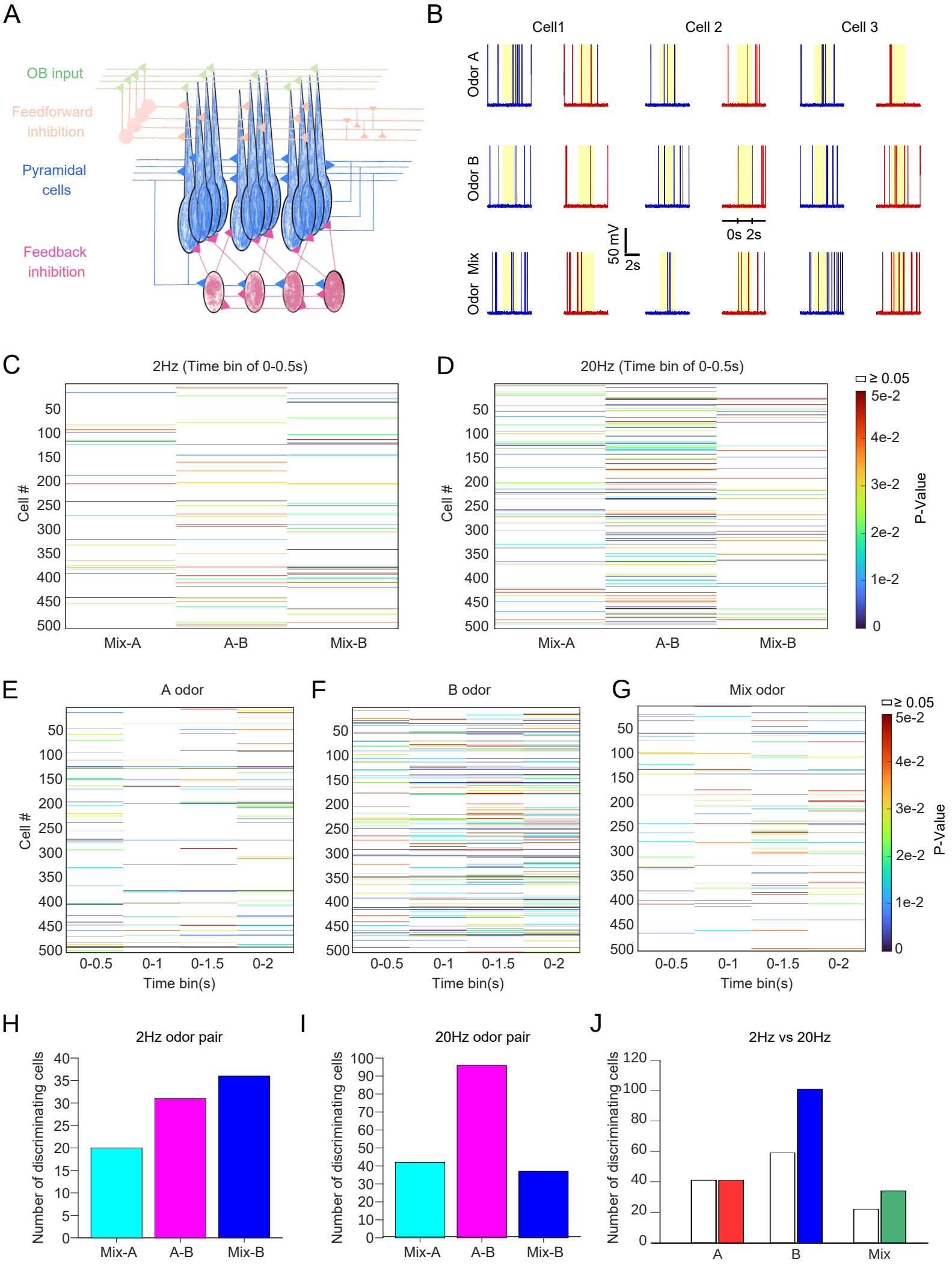
A
OB input
Feedforward inhibition
Pyramidal cells
Feedback inhibition
B
Cell1
Cell 2
Cell 3
Odor A
Odor B
Odor Mix
50 mV
2s
0s 2s
C
2Hz (Time bin of 0-0.5s)
Cell #
Mix-A
A-B
Mix-B
D
20Hz (Time bin of 0-0.5s)
≥ 0.05
5e-2
4e-2
3e-2
2e-2
1e-2
0
P-Value
E
A odor
F
B odor
G
Mix odor
0-0.5
0-1
0-1.5
0-2
Time bin(s)
H
2Hz odor pair
Number of discriminating cells
I
20Hz odor pair
J
2Hz vs 20Hz
A
B
Mix

Figure 2

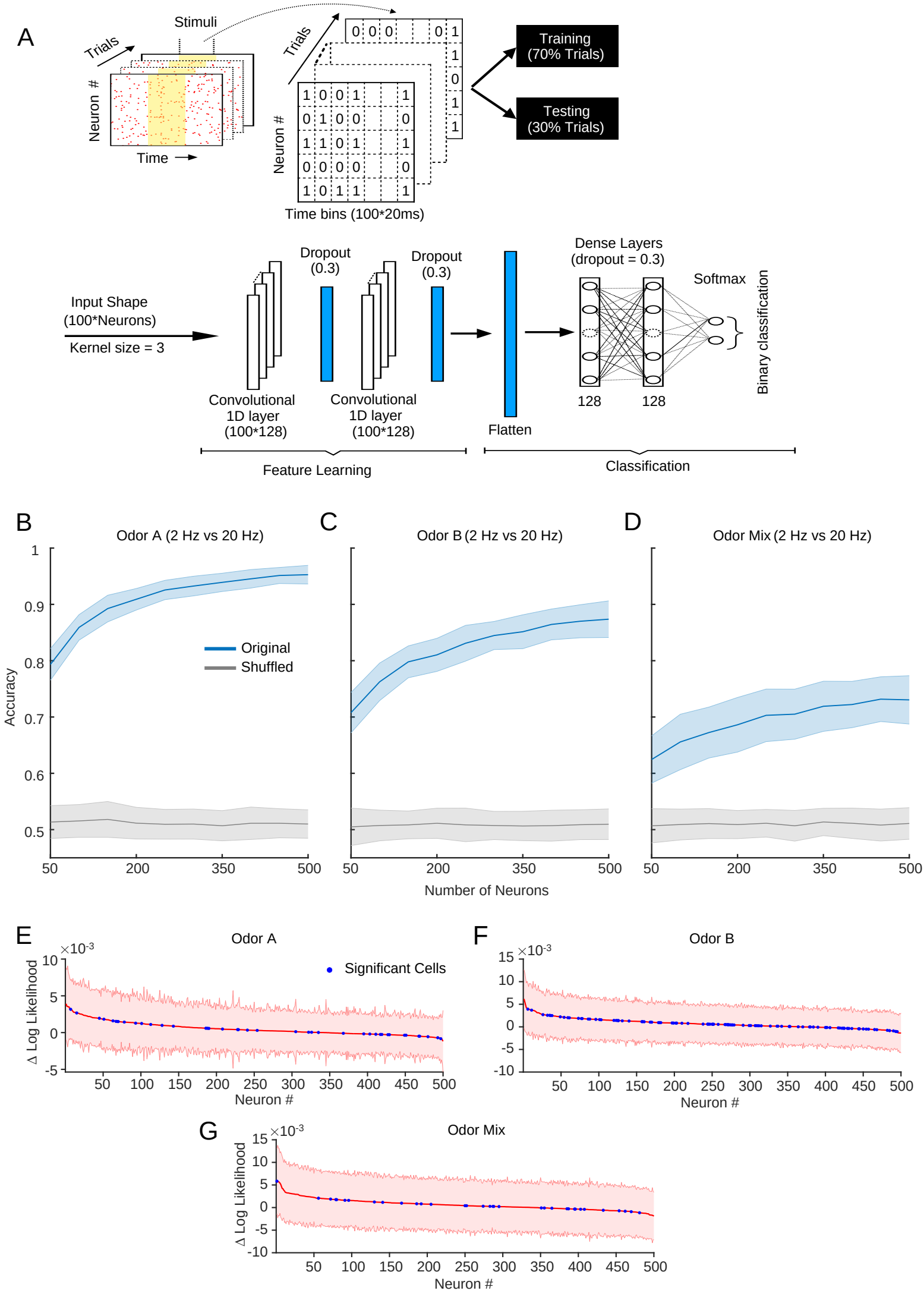
A
Stimuli
Trials
Neuron #
Time
Trials
Neuron #
Time bins (100*20ms)
Training
(70% Trials)
Testing
(30% Trials)
Input Shape
(100*Neurons)
Kernel size = 3
Convolutional
1D layer
(100*128)
Dropout
(0.3)
Convolutional
1D layer
(100*128)
Dropout
(0.3)
Flatten
Dense Layers
(dropout = 0.3)
128
128
Softmax
Binary classification
Feature Learning
Classification
B
Odor A (2 Hz vs 20 Hz)
C
Odor B (2 Hz vs 20 Hz)
D
Odor Mix (2 Hz vs 20 Hz)
Accuracy
Original
Shuffled
Number of Neurons
E
Odor A
Significant Cells
Δ Log Likelihood
Neuron #
F
Odor B
Neuron #
G
Odor Mix
Δ Log Likelihood
Neuron #

Figure 3

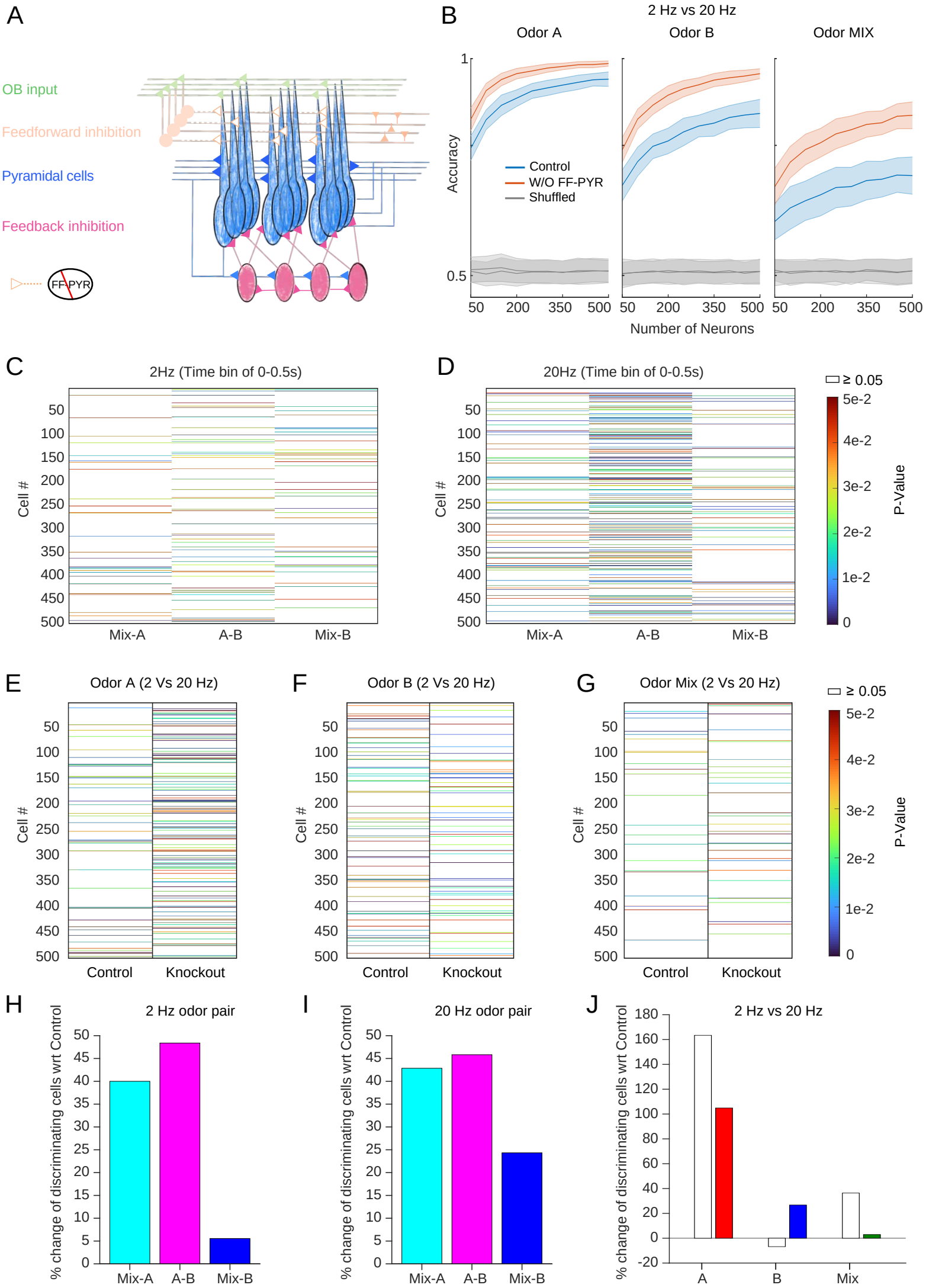
A
OB input
Feedforward inhibition
Pyramidal cells
Feedback inhibition
FF-PYR
B
2 Hz vs 20 Hz
Odor A
Odor B
Odor MIX
Accuracy
Control
W/O FF-PYR
Shuffled
Number of Neurons
C
2Hz (Time bin of 0-0.5s)
Cell #
Mix-A
A-B
Mix-B
D
20Hz (Time bin of 0-0.5s)
≥ 0.05
P-Value
E
Odor A (2 Vs 20 Hz)
Control
Knockout
F
Odor B (2 Vs 20 Hz)
G
Odor Mix (2 Vs 20 Hz)
H
2 Hz odor pair
% change of discriminating cells wrt Control
I
20 Hz odor pair
J
2 Hz vs 20 Hz
A
B
Mix

Figure 4

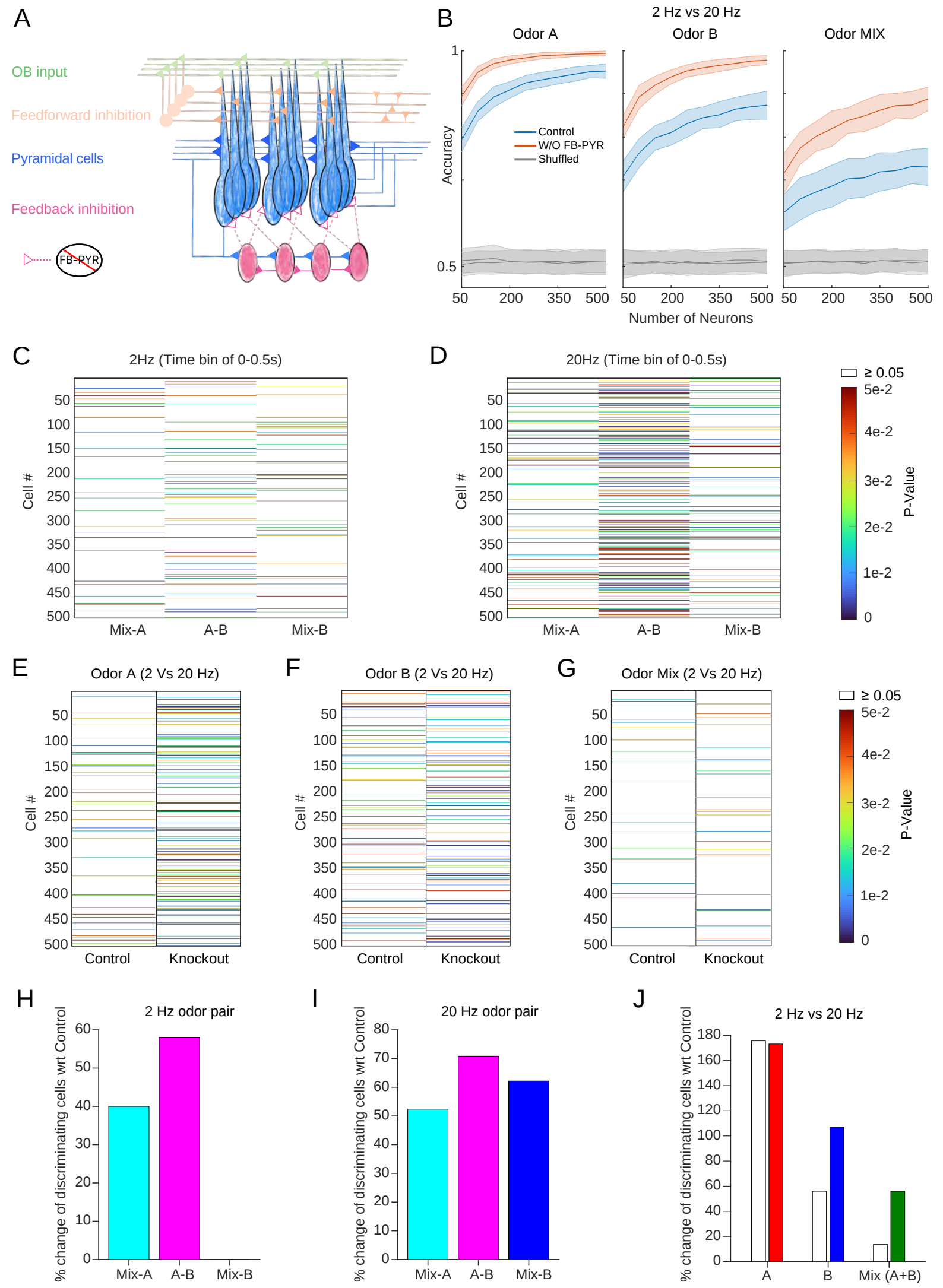
A
OB input
Feedforward inhibition
Pyramidal cells
Feedback inhibition
FB-PYR
B
2 Hz vs 20 Hz
Odor A
Odor B
Odor MIX
Accuracy
Control
W/O FB-PYR
Shuffled
Number of Neurons
C
2Hz (Time bin of 0-0.5s)
Cell #
Mix-A
A-B
Mix-B
D
20Hz (Time bin of 0-0.5s)
≥ 0.05
P-Value
E
Odor A (2 Vs 20 Hz)
Control
Knockout
F
Odor B (2 Vs 20 Hz)
G
Odor Mix (2 Vs 20 Hz)
H
2 Hz odor pair
% change of discriminating cells wrt Control
I
20 Hz odor pair
J
2 Hz vs 20 Hz
A
B
Mix (A+B)

Figure 5

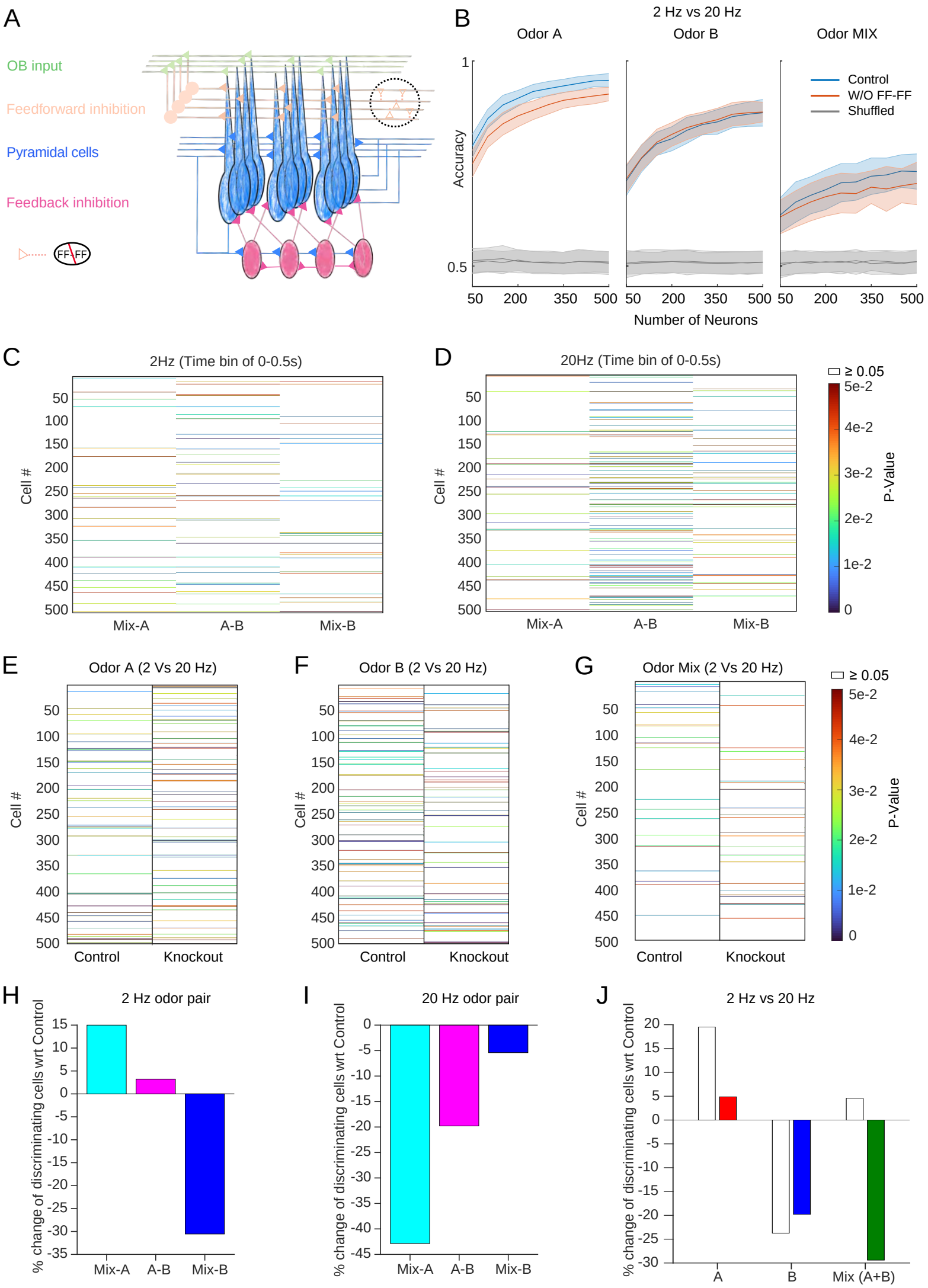
A
OB input
Feedforward inhibition
Pyramidal cells
Feedback inhibition
FF
FF
B
2 Hz vs 20 Hz
Odor A
Odor B
Odor MIX
Control
W/O FF-FF
Shuffled
Accuracy
1
0.5
50
200
350
500
Number of Neurons
C
2Hz (Time bin of 0-0.5s)
Cell #
Mix-A
A-B
Mix-B
D
20Hz (Time bin of 0-0.5s)
≥ 0.05
5e-2
4e-2
3e-2
2e-2
1e-2
0
P-Value
E
Odor A (2 Vs 20 Hz)
Control
Knockout
F
Odor B (2 Vs 20 Hz)
G
Odor Mix (2 Vs 20 Hz)
H
2 Hz odor pair
% change of discriminating cells wrt Control
I
20 Hz odor pair
J
2 Hz vs 20 Hz
A
B
Mix (A+B)

Figure 6

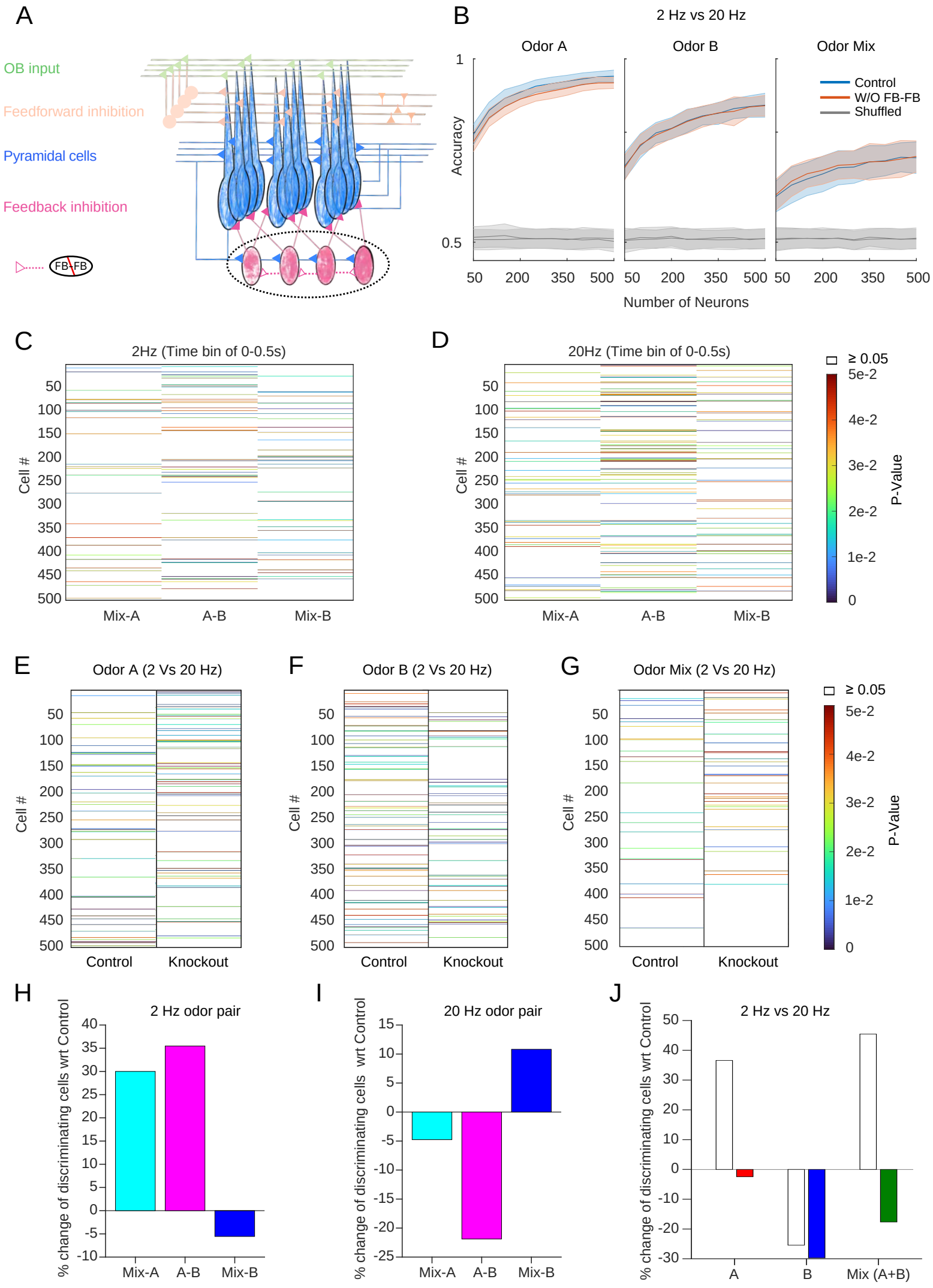
A
OB input
Feedforward inhibition
Pyramidal cells
Feedback inhibition
FB-FB
B
2 Hz vs 20 Hz
Odor A
Odor B
Odor Mix
Control
W/O FB-FB
Shuffled
Accuracy
1
0.5
50 200 350 500
Number of Neurons
C
2Hz (Time bin of 0-0.5s)
Cell #
Mix-A
A-B
Mix-B
D
20Hz (Time bin of 0-0.5s)
≥ 0.05
5e-2
4e-2
3e-2
2e-2
1e-2
0
P-Value
E
Odor A (2 Vs 20 Hz)
Control
Knockout
F
Odor B (2 Vs 20 Hz)
G
Odor Mix (2 Vs 20 Hz)
H
2 Hz odor pair
% change of discriminating cells wrt Control
I
20 Hz odor pair
J
2 Hz vs 20 Hz
A
B
Mix (A+B)

Figure 7

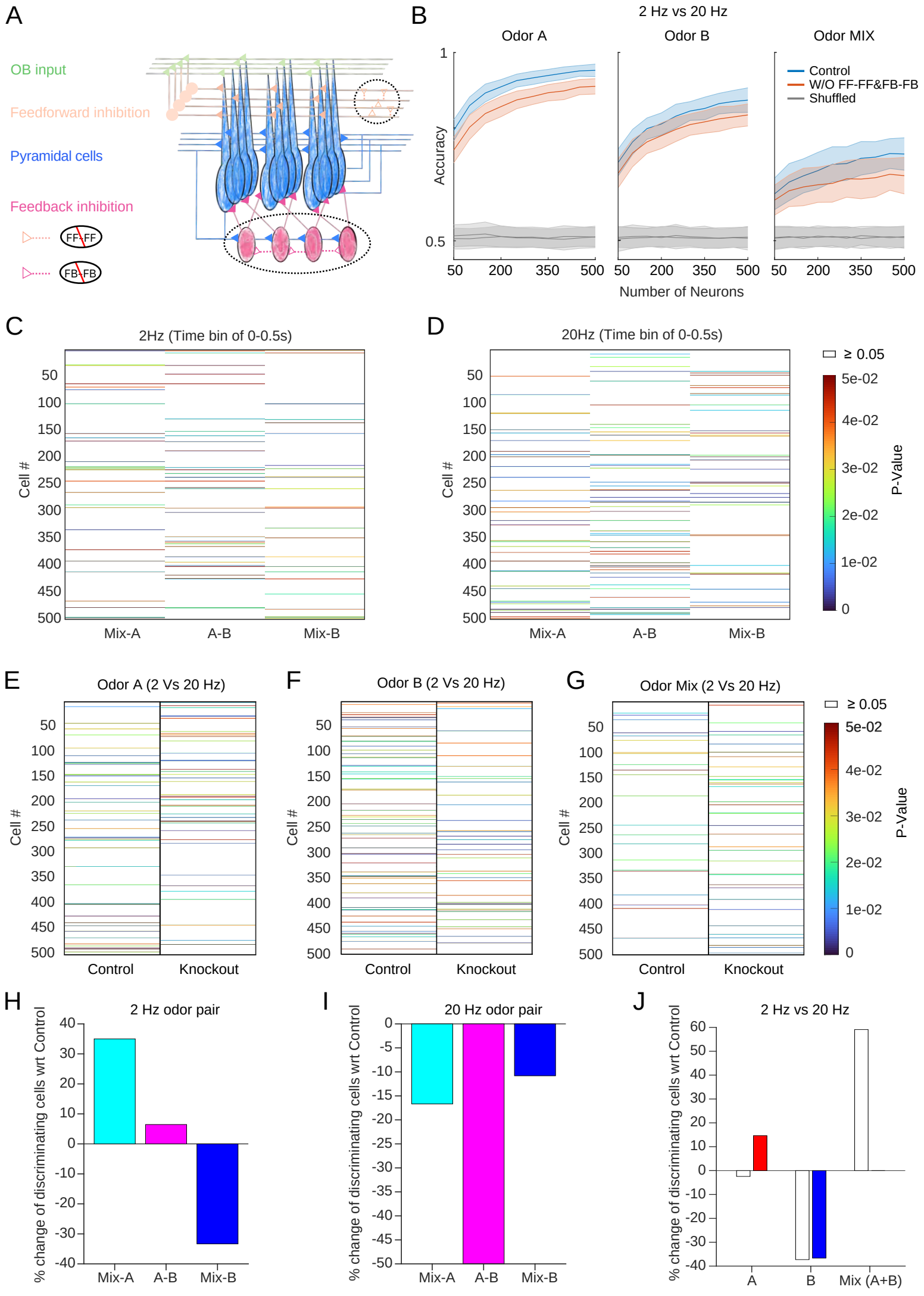
A
OB input
Feedforward inhibition
Pyramidal cells
Feedback inhibition
FF-FF
FB-FB
B
2 Hz vs 20 Hz
Odor A
Odor B
Odor MIX
Control
W/O FF-FF&FB-FB
Shuffled
Accuracy
Number of Neurons
C
2Hz (Time bin of 0-0.5s)
Cell #
Mix-A
A-B
Mix-B
D
20Hz (Time bin of 0-0.5s)
≥ 0.05
P-Value
E
Odor A (2 Vs 20 Hz)
Control
Knockout
F
Odor B (2 Vs 20 Hz)
G
Odor Mix (2 Vs 20 Hz)
H
2 Hz odor pair
% change of discriminating cells wrt Control
I
20 Hz odor pair
J
2 Hz vs 20 Hz
A
B
Mix (A+B)

Figure 8

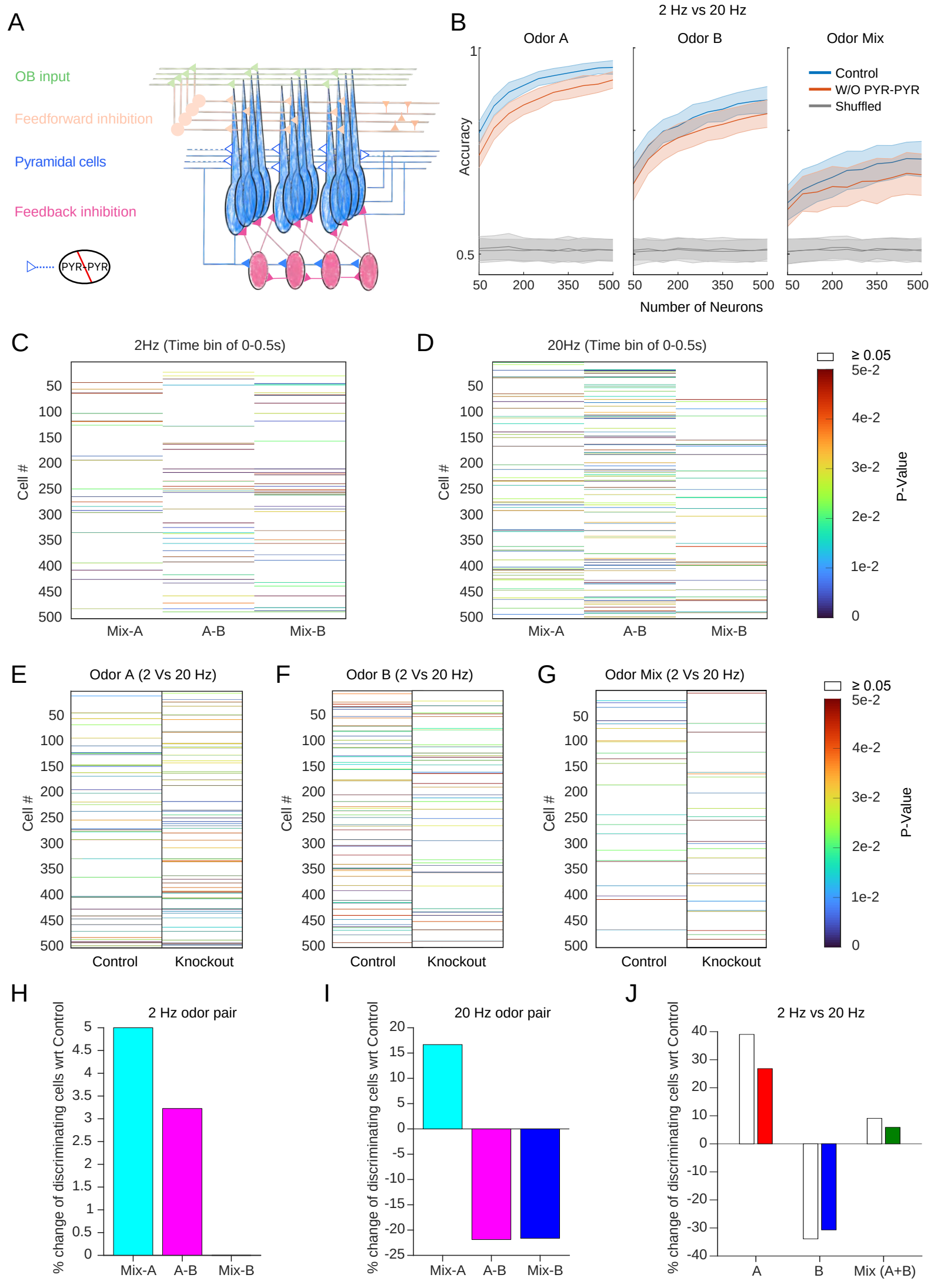
A
OB input
Feedforward inhibition
Pyramidal cells
Feedback inhibition
PYR-PYR
B
2 Hz vs 20 Hz
Odor A
Odor B
Odor Mix
Control
W/O PYR-PYR
Shuffled
Accuracy
1
0.5
50
200
350
500
Number of Neurons
C
2Hz (Time bin of 0-0.5s)
Cell #
Mix-A
A-B
Mix-B
D
20Hz (Time bin of 0-0.5s)
≥ 0.05
5e-2
4e-2
3e-2
2e-2
1e-2
0
P-Value
E
Odor A (2 Vs 20 Hz)
Control
Knockout
F
Odor B (2 Vs 20 Hz)
G
Odor Mix (2 Vs 20 Hz)
H
2 Hz odor pair
% change of discriminating cells wrt Control
I
20 Hz odor pair
J
2 Hz vs 20 Hz
A
B
Mix (A+B)

Figure 9

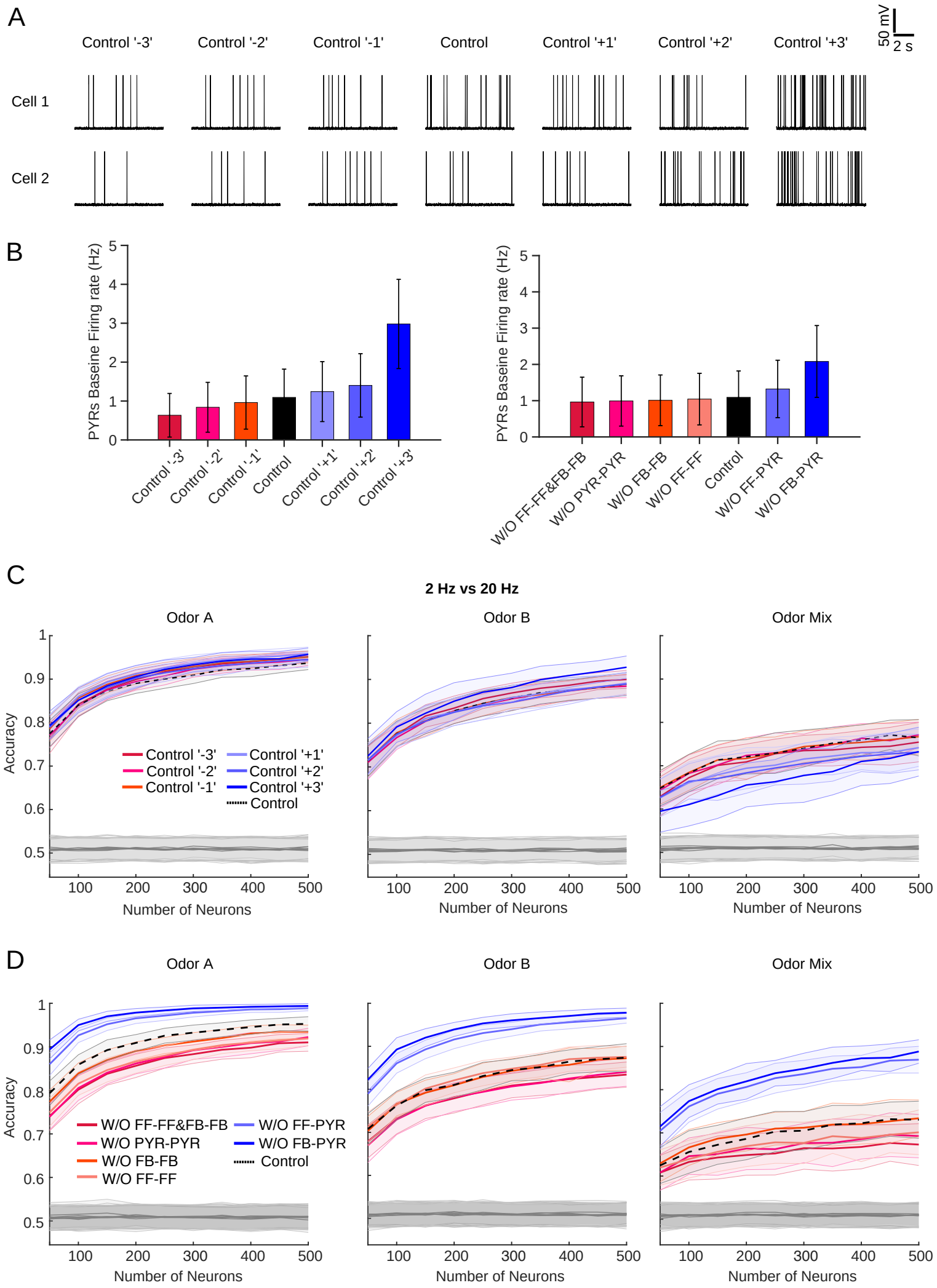
A
Control '-3'
Control '-2'
Control '-1'
Control
Control '+1'
Control '+2'
Control '+3'
50 mV
2 s
Cell 1
Cell 2
B
PYRs Baseine Firing rate (Hz)
Control '-3'
Control '-2'
Control '-1'
Control
Control '+1'
Control '+2'
Control '+3'
W/O FF-FF&FB-FB
W/O PYR-PYR
W/O FB-FB
W/O FF-FF
W/O FF-PYR
W/O FB-PYR
C
2 Hz vs 20 Hz
Odor A
Odor B
Odor Mix
Accuracy
Number of Neurons
D

Table 1

Parameters	PYR						FFIN	FBIN
	Soma	Dend1	Dend2	Dend3	Dend4	Dend5	Soma	Soma
Input Resistance (MΩ)	79.84	80.28	84.94	99.36	137.58	246.18	93.36	50.29
Avg. spontaneous firing rate (mean ± std) (Hz)	2.22±0.98	2.21±1.27	2.32±1.2	2.19±1.16	2.2±1.4	2.67±1.59	2±1.14	6.55±2.11
Length (µm)	100	100	100	100	100	100	85	68
Diameter (µm)	29	2.57	1.77	1.2	0.8	0.5	85	68

Table 2

Synaptic Connections	Synaptic Weight	EPSP/IPSP w.r.t RMP (mV)	Tau1 (ms)	Tau 2 (ms)	E_N (mV)	Synaptic Latency (ms)	Connection Probability
PYR-PYR DEND 1	0.00002	0.12	0.24	3.6	0	1.54	0.2
PYR-PYR DEND 2	0.00002	0.11	0.24	3.6	0	1.54	
PYR-PYR DEND 3	0.00002	0.11	0.24	3.6	0	1.54	
PYR-PYR DEND 4	0.00002	0.11	0.24	3.6	0	1.54	
FBIN-PYR SOMA	0.007	1.9	0.2	1.2	-80	0.65	0.35
FFIN-PYR DEND 4	0.007	1.4	0.2	1.2	-80	0.6	0.3
FFIN-PYR DEND 5	0.007	0.95	0.2	1.2	-80	0.6	
FBIN-FBIN	0.06	1.5	0.2	1.2	-80	1.54	0.1
PYR-FBIN	0.0001	0.31	0.26	9	0	0.65	0.18
M/T-PYR DEND 5	0.000037	0.19	0.2	1.2	0	1.27	0.2
M/T-FFIN	0.00015	0.59	0.2	1.2	0	2.42	0.4
FFIN-FFIN	0.0095	3	0.2	1.2	-80	1.54	0.4

Table 3

Condition	Original			Shuffle		
	A	B	MIX	A	B	MIX
Control	0.953 ± 0.017	0.874 ± 0.033	0.73 ± 0.043	0.51 ± 0.025	0.51 ± 0.027	0.511 ± 0.028
W/O FB-PYR	0.994 ± 0.005	0.978 ± 0.011	0.888 ± 0.027	0.51 ± 0.03	0.511 ± 0.028	0.512 ± 0.027
W/O FF-PYR	0.989 ± 0.006	0.965 ± 0.011	0.869 ± 0.031	0.511 ± 0.027	0.509 ± 0.029	0.51 ± 0.03
W/O FF-FF	0.919 ± 0.016	0.875 ± 0.024	0.701 ± 0.052	0.507 ± 0.028	0.509 ± 0.027	0.51 ± 0.027
W/O FB-FB	0.935 ± 0.015	0.872 ± 0.028	0.734 ± 0.042	0.502 ± 0.029	0.51 ± 0.027	0.509 ± 0.027
W/O PYR-PYR	0.922 ± 0.02	0.84 ± 0.033	0.693 ± 0.05	0.509 ± 0.027	0.512 ± 0.024	0.508 ± 0.027
W/O FF-FF + FB-FB	0.91 ± 0.02	0.834 ± 0.029	0.673 ± 0.048	0.51 ± 0.029	0.507 ± 0.031	0.508 ± 0.029

Table 4

W/O FF-FF&FB-FB	W/O PYR-PYR	W/O FB-FB	W/O FF-FF	CONTROL	W/O FF-PYR	W/O FB-PYR
0.963±0.683	0.992±0.692	1.01±0.699	1.04±0.711	1.09±0.726	1.32±0.792	2.08±0.991
Control ‘-3’	Control ‘-2’	Control ‘-1’	Control	Control ‘+1’	Control ‘+2’	Control ‘+3’
0.635±0.561	0.839±0.641	0.961±0.683	1.09±0.726	1.24±0.771	1.4±0.815	2.98±1.146